LhARA: The Laser-hybrid Accelerator for Radiobiological Applications

G. Aymar [1], **T. Becker** [2], **S. Boogert** [3], **M. Borghesi** [4], **R. Bingham** [5,1],

C. Brenner [1], **P. Burrows** [6], **O.C. Ettlinger** [7], **T. Dascalu** [7], **S. Gibson** [3],

T. Greenshaw [8], **S. Gruber** [9], **D. Gujral** [10], **C. Hardiman** [10], **J. Hughes** [8],

W.G. Jones [7,18], **K. Kirkby** [11], **A. Kurup** [7,*], **J-B. Lagrange** [1], **K. Long** [7,1], **W. Luk** [7],

J. Matheson [1], **P. Mckenna** [5], **R. Mclauchlan** [10], **Z. Najmudin** [7], **H.T. Lau** [7],

J. Parsons [8], **J. Pasternak** [7,1], **J. Pozimski** [7,1], **K. Prise** [4], **P. Ratoff** [12],

G. Schettino [13,17], **W. Shields** [3], **S. Smith** [14], **J. Thomason** [1], **S. Towe** [15],

P. Weightman [8], **C. Whyte** [5], **R. Xiao** [16]

[1] *STFC Rutherford Appleton Laboratory, Harwell Oxford, Didcot, OX11 0QX, UK*

[2] *Maxeler technologies Limitted, 3 Hammersmith Grove, London W6 0ND, UK*

[3] *Royal Holloway, University of London, Egham, Surrey, TW20 0EX, UK*

[4] *Queens University Belfast, University Road, Belfast, BT7 1NN, Northern Ireland, UK*

[5] *University of Stratchclyde, 16 Richmond Street, Glasgow, G1 1XQ, UK*

[6] *The John Adams Institute, Denys Wilkinson Building, Keble Road, Oxford OX1 3RH, UK*

[7] *Imperial College London, Exhibition Road, London, SW7 2AZ, UK*

[8] *University of Liverpool, Liverpool L3 9TA, UK*

[9] *Christian Doppler Laboratory for Medical Radiation Research for Radiation Oncology, Medical University of Vienna, Spitalgasse 23, 1090 Vienna, Austria*

[10] *Imperial College NHS Healthcare Trust, The Bays, South Wharf Road, St Mary's Hospital, London W2 1NY, UK*

[11] *University of Manchester, Oxford Road, Manchester, M13 9PL, UK*

[12] *The Cockcroft Institute Daresbury Laboratory, Sci-Tech Daresbury, Daresbury, Warrington, WA4 4AD, UK*

[13] *National Physical Laboratory, Hampton Road, Teddington, Middlesex, TW11 0LW, UK*

[14] *STFC Daresbury Laboratory, Daresbury, Cheshire, WA4 4AD, UK*

[15] *Leo Cancer Care, Broadview, Windmill Hill, Hailsham, East Sussex, BN27 4RY, UK*

[16] *Cororain, 14F, Changfu Jinmao Building (CFC), Trade-free Zone, Futian District, Shenzhen, Guangdong, China*

[17] *University of Surrey, 388 Stag Hill, Guilford, GU2 7XH, UK*

[18] *Imperial Patient and Public Involvement Group (IPPIG), Imperial College London, Exhibition Road, London, SW7 2AZ, UK*

Correspondence*:
A. Kurup
a.kurup@imperial.ac.uk

2 ABSTRACT

3 The 'Laser-hybrid Accelerator for Radiobiological Applications', LhARA, is conceived as a novel,
4 uniquely-flexible facility dedicated to the study of radiobiology. The technologies demonstrated
5 in LhARA, which have wide application, may be developed to allow particle-beam therapy to be
6 delivered in a completely new regime, combining a variety of ion species in a single treatment
7 fraction and exploiting ultra-high dose rates. LhARA will be a hybrid accelerator system in which
8 laser interactions drive the creation of a large flux of protons or light ions that are captured using
9 a plasma (Gabor) lens and formed into a beam. The laser-driven source allows protons and ions
10 to be captured at energies significantly above those that pertain in conventional facilities, thus
11 evading the current space-charge limit on the instantaneous dose rate that can be delivered. The
12 laser-hybrid approach, therefore, will allow radiobiological studies to be carried out in completely
13 new regimes, delivering protons and light ions in a wide variety of time structures, spectral
14 distributions, and spatial configurations at instantaneous dose rates up to and significantly beyond
15 the ultra-high dose-rate 'FLASH' regime.

16 It is proposed that LhARA be developed in two stages. In the first stage, a programme of in-vitro
17 experiments will be served with proton beams with energies between 10 MeV and 15 MeV. In
18 stage two, the beam will be accelerated using a fixed-field accelerator (FFA). This will allow
19 experiments to be carried out in vitro and in vivo with proton beam energies of up to 125 MeV. In
20 addition, ion beams with energies up to 30 MeV per nucleon will be available for in-vitro an in-vivo
21 experiments. This paper presents the conceptual design for LhARA and the R&D programme by
22 which the LhARA consortium seeks to establish the facility.

23 LAY SUMMARY

24 It is well established that radiation therapy (RT) is an effective treatment for many types of cancer.
25 Most treatments are delivered by machines that accelerate electrons which are then used to
26 produce a beam of high energy photons (high energy X-rays) which are directed at a tumour
27 to kill cancer cells. However, healthy tissue anywhere in the path of the photon beam is also
28 irradiated and so can be damaged, although there are ways of reducing this damage by using
29 several beams at different angles.

30 Recent years have seen the use of a new type of machine in which protons are accelerated to
31 produce proton beams (rather than photon beams) which are directed at a tumour. These proton
32 beams can be arranged to deposit almost all of their energy in a small volume within a tumour so
33 they cause little damage to healthy tissue; a major advantage over photon beams. But proton
34 machines are large and expensive, so there is a need for the development of proton machines
35 that are smaller, cheaper and more flexible in how they can be used.

36 The LhARA project is aimed at the development of such proton machines using a new approach
37 based on high powered lasers. Such new machines could also make it easier to deliver the dose
38 in very short high-intensity pulses and as a group of micro-beams—exciting recent research has
39 shown that this brings improved effectiveness in killing cancer cells while sparing healthy tissue.
40 The technology to be proved in LhARA should enable a course of RT to be delivered in days
41 rather than weeks and should be more effective.

42 Scientifically, there is a need to understand much better the basic processes by which radiation
43 interacts with biological matter to kill cancer cells—the investigation of these processes involves
44 physics as well as biology. Thus the most important aim of LhARA is to pursue this radiobiological

45 research in new regimes and from this to develop better treatments. LhARA will also pursue
46 technological research into laser-hybrid accelerators.

47 **Keywords: Radiobiology, Novel acceleration, Laser-driven acceleration, Plasma lens, Fixed field alternating gradient acceleration**

1 INTRODUCTION

Cancer is the second most common cause of death globally [The World Health Organisation (2020)]. In 2018, 18.1 million new cancer cases were diagnosed, 9.6 million people died of cancer-related disease, and 43.8 million people were living with cancer [Bray et al. (2018); Fitzmaurice et al. (2018)]. It is estimated that 26.9 million life-years could be saved in low- and middle-income countries if radiotherapy capacity could be scaled up [Atun et al. (2015)]. Novel techniques incorporated in facilities that are at once robust, automated, efficient, and cost-effective are required to deliver the required scale-up in provision.

Radiation therapy (RT), a cornerstone of cancer treatment, is used in over 50% of cancer patients [Datta et al. (2019)]. The most frequently used types of radiotherapy employ photon or electron beams with MeV-scale energies. Proton and ion beams offer substantial advantages over X-rays because the bulk of the beam energy is deposited in the Bragg peak. This allows dose to be conformed to the tumour while sparing healthy tissue and organs at risk. The benefits of proton and ion-beam therapy (PBT) are widely recognised. PBT today is routinely delivered in fractions of ~ 2 Gy per day over several weeks; each fraction being delivered at a rate of $\lesssim 10$ Gy/min deposited uniformly over the target treatment volume. Exciting evidence of therapeutic benefit has recently been reported when dose is delivered at ultra-high dose-rate, $\gtrsim 40$ Gy/s ("FLASH" RT) [Favaudon et al. (2014); Vozenin et al. (2019)], or provided in multiple micro-beams with diameter less than 1 mm distributed over a grid with inter-beam spacing of ~ 3 mm [Prezado et al. (2017)]. However, the radiobiological mechanisms by which the therapeutic benefit is generated are not properly understood.

LhARA, the Laser-hybrid Accelerator for Radiobiological Applications is conceived as the new, highly flexible, source of radiation that is required to explore the vast "terra incognita" of the mechanisms by which the biological response to ionising radiation is determined by the physical characteristics of the beam. A high-power pulsed laser will be used to drive the creation of a large flux of protons or light ions which are captured and formed into a beam by strong-focusing plasma lenses. The laser-driven source allows protons and ions to be captured at energies significantly above those that pertain in conventional facilities, thus evading the current space-charge limit on the instantaneous dose rate that can be delivered. The plasma (Gabor) lenses provide the same focusing strength as high-field solenoids at a fraction of the cost. Rapid acceleration will be performed using a fixed-field alternating-gradient accelerator (FFA) thereby preserving the unique flexibility in the time, energy, and spatial structure of the beam afforded by the laser-driven source.

We propose that LhARA be developed in two stages. In the first stage, the laser-driven beam, captured and transported using plasma lenses and bending magnets, will serve a programme of in-vitro experiments with proton beams of energy of up to 15 MeV. In stage two, the beam will be accelerated using a fixed-field accelerator (FFA). This will allow experiments to be carried out in vitro and in vivo with proton-beam energies of up to 125 MeV. Ion beams (including C^{6+}) with energies up to 30 MeV per nucleon will also be available.

The laser pulse that initiates the production of protons or ions at LhARA may be triggered at a repetition rate of up to 10 Hz. The time structure of the beam may therefore be varied to interrupt the chemical and biological pathways that determine the biological response to ionising radiation with 10 ns to 40 ns long proton or ion bunches repeated at intervals as small as 100 ms. The technologies chosen to capture, transport, and accelerate the beam in LhARA have been made so that this unique capability is preserved. The LhARA beam may be used to deliver an almost uniform dose distribution over a circular area with a maximum diameter of between 1 cm and 3 cm. Alternatively the beam can be focused to a spot with diameter of ~ 1 mm.

91 The technologies demonstrated in LhARA have the potential to be developed to make "best in class"
92 treatments available to the many by reducing the footprint of future particle-beam therapy systems. The
93 laser-hybrid approach, therefore, will allow radiobiological studies and eventually radiotherapy to be
94 carried out in completely new regimes, delivering a variety of ion species in a broad range of time
95 structures, spectral distributions, and spatial configurations at instantaneous dose rates up to and potentially
96 significantly beyond the current ultra-high dose-rate "FLASH" regime.

97 The LhARA consortium is the multidisciplinary collaboration of clinical oncologists, medical and
98 academic physicists, biologists, engineers, and industrialists required to deliver such a transformative
99 particle-beam system. With its "pre Conceptual Design Report" (pre-CDR) [The LhARA consortium
100 (2020)] the consortium lays out its concept for LhARA, its potential to serve a ground-breaking programme
101 of radiobiology, and the technological advances that will be made in its execution. The work presented in
102 the LhARA pre-CDR lays the foundations for the development of full conceptual and technical designs
103 for the facility. The pre-CDR also contains a description of the R&D that is required to demonstrate the
104 feasibility of critical components and systems. This paper presents a summary of the contents of the
105 pre-CDR and lays out the vision of the consortium.
106

2 MOTIVATION

107 Conventional (X-ray) RT is one of the most effective cancer treatments, particularly for solid tumours
108 including head and neck tumours and glioblastoma. The dose delivered using X-rays falls exponentially
109 with depth; this characteristic implies a fundamental limit on the maximum dose that can be delivered to
110 the tumour without delivering an unacceptably large dose to healthy tissue. Tumours that lie deep within
111 the patient will receive a dose significantly lower than that delivered to the healthy tissues through which
112 the beam passes on its way to the treatment site. X-rays that pass through the tumour will also deliver a
113 dose to the tissues that lie behind. Dose delivered to healthy tissues can cause the death of the healthy cells
114 and create adverse side effects. Furthermore, the maximum X-ray dose that can be delivered is limited by
115 the presence of sensitive organs such as the brain and spinal cord. This situation is particularly acute in
116 infants for whom dose to healthy tissue, sensitive organs, and bone can lead to developmental issues and a
117 higher probability of secondary malignancies later in life. The efficacy of X-ray therapy is also impacted by
118 biological factors such as the tumour micro-environment, the oxygen level (hypoxia) present in the tissue,
119 and the inherent radio-resistance of certain types of tumour.

120 RT delivered using protons and ions, particle-beam therapy (PBT), has the potential to overcome the
121 fundamental limitation of X-rays in cancer treatment [Loeffler and Durante (2013)]. The physics of the
122 interaction between ionising radiation and tissue determines the radiobiological effect. Energy loss through
123 ionisation is the dominant mechanism at the beam energies relevant to proton- or ion-beam therapy. The
124 energy lost per unit distance travelled (the linear energy transfer, LET) increases as the proton or ion slows
125 down. At low velocity the rate of increase in LET is extremely rapid. This generates a 'Bragg peak' in the
126 energy deposited at the maximum range of the beam just as the protons or ions come to rest. In contrast to
127 photons, this characteristic allows the dose delivered to healthy tissue behind the Bragg peak to be reduced
128 to zero for protons, and almost to zero for carbon ions. The effect of scanning the Bragg peak over the
129 tumour volume is to increase the dose to the tumour while, in comparison to X-ray therapy, sparing tissues
130 in front of the tumour. By choosing carefully the treatment fields, dose to sensitive organs can be reduced
131 significantly compared to an equivalent treatment with photons, thus improving patient outcomes. The
132 Particle Therapy Co-Operative Group (PTCOG) currently lists 90 proton therapy facilities and 12 carbon
133 ion therapy facilities, and these are located predominantly in high-income countries [PTCOG (2020)]. Low-

134 and middle-income countries (LMIC) are relatively poorly served, indeed nearly 70% of cancer patients
135 globally do not have access to RT [Datta et al. (2019)]. Novel RT techniques incorporated in facilities that
136 are robust, automated, efficient, and cost-effective are therefore required to deliver the necessary scale-up
137 in provision. This presents both a challenge and an opportunity; developing the necessary techniques
138 and scaling up RT provision will require significant investment but will also create new markets, drive
139 economic growth through new skills and technologies and deliver impact through improvements in health
140 and well-being.

The case for a systematic study of the radiobiology of proton and ion beams

142 The nature of the particle-tissue interaction confers on PBT the advantage that the dose can be precisely
143 controlled and closely conformed to the tumour volume. However, there are significant biological
144 uncertainties in the impact of ionising radiation on living tissue. The efficacy of proton and ion beams is
145 characterised by their relative biological effectiveness (RBE) in comparison to reference photon beams.
146 The treatment-planning software that is in use in the clinic today assumes an RBE value for protons of
147 1.1 [Paganetti and van Luijk (2013)]. This means that a lower dose of protons is needed to produce the
148 same therapeutic effect that would be obtained using X-rays. However, the rapid rise in the LET at the
149 Bragg peak leads to significant uncertainties in the RBE. It is known that RBE depends strongly on many
150 factors, including particle energy, dose, dose rate, the degree of hypoxia, and tissue type [Paganetti (2014)],
151 however, the radiobiology that determines these dependencies is not fully understood. A number of studies
152 have shown that there can be significant variation in RBE [Jones et al. (2018); Giovannini et al. (2016); Lühr
153 et al. (2018)]. Indeed, RBE values from 1.1 to over 3 have been derived from in-vitro clonogenic survival
154 assay data following proton irradiation of cultured cell lines derived from different tumours [Paganetti
155 (2014); Chaudhary et al. (2014); Wilkens and Oelfke (2004)]. Some of this variation may be due to the
156 positioning of the cells during irradiation relative to the Bragg peak. RBE values of ~ 3 are accepted for
157 high-LET carbon-ion irradiation, although higher values have been reported [Karger and Peschke (2017)].
158 RBE uncertainties for carbon and other ion species are at least as large as they are for protons.

159 Uncertainties in RBE can lead to a mis-estimation of the dose required to treat a particular tumour.
160 Overestimation of the required dose leads to risk of damage to healthy tissue, while an underestimate can
161 lead to the tumour not being treated sufficiently for it to be eradicated. RT causes cell death by causing
162 irreparable damage to the cell's DNA. Hence, differences in RBE can also affect the spectrum of DNA
163 damage induced within tumour cells. The larger RBE values corresponding to higher LET, can cause
164 increases in the frequency and complexity of DNA damage, particularly DNA double strand breaks (DSB)
165 and complex DNA damage (CDD) where multiple DNA lesions are induced in close proximity [Vitti and
166 Parsons (2019a); Carter et al. (2018)]. These DNA lesions are a major contributor to radiation-induced cell
167 death as they represent a significant barrier to the cellular DNA repair machinery. Furthermore, the specific
168 nature of the DNA damage induced by ions determines the principal DNA repair pathways employed to
169 effect repair; base excision repair is employed in response to DNA-base damage and single-strand breaks,
170 while non-homologous end-joining and homologous recombination is employed in response to DSBs [Vitti
171 and Parsons (2019b)]. However, there are a number of other biological factors that contribute greatly to RBE
172 in specific tumours, including the intrinsic radio-sensitivity of the tissue, the level of oxygenation (hypoxia),
173 the growth and repopulation characteristics, and the associated tumour micro-environment. Consequently,
174 there is significant uncertainty in the precise radiobiological mechanisms that arise following PBT and a
175 more detailed and precise understanding is required for optimal patient-treatment strategies to be devised.
176 Detailed systematic studies of the biophysical effects of the interaction of protons and ions, under different
177 physical conditions, with different tissue types will provide important information on RBE variation and
178 could enable enhanced treatment-planning algorithms to be devised. In addition, studies examining the

179 impact of combination therapies with PBT (e.g. targeting the DNA damage response, hypoxia signalling
180 mechanisms and also the tumour micro-environment) are currently sparse, and performing these is vital in
181 devising future personalised patient-therapy strategies using PBT. Such studies are needed, especially in
182 the case of ion-beam radiotherapy.

183 **The case for novel beams for radiobiology**
184 PBT delivery to date has been restricted to a small number of beam characteristics. In a typical treatment
185 regimen the therapeutic dose is provided in a series of daily sessions delivered over a period of several
186 weeks. Each session would consist of the delivery of a single fraction of ~ 2 Gy delivered at a rate of
187 $\lesssim 5$ Gy/minute. The dose in each fraction would be distributed uniformly over an area of several square
188 centimetres. Exciting evidence of therapeutic benefit has recently been reported when the dose is delivered
189 at ultra-high dose rates (> 40 Gy/s) and termed FLASH RT [Favaudon et al. (2014); Vozenin et al. (2019)].
190 These studies indicate significantly reduced lung fibrosis in mice and skin toxicity in mini-pigs, and reduced
191 side-effects in cats with nasal squamous-cell carcinoma. Varian has indicated that dose rates greater than
192 40 Gy/s are useful for FLASH irradiation [Systems (2020)], while IBA have indicated that the FLASH
193 phenomenon is observed at dose rates above 33 Gy/s [IBA (2019)]. In addition, therapeutic benefit has
194 been demonstrated with the use of multiple micro-beams with diameter of less than 1 mm distributed over a
195 grid with inter-beam spacing of 3 mm [Prezado et al. (2017)]. However, there is still significant uncertainty
196 of the thresholds and the radiobiological mechanisms by which therapeutic benefit is generated in FLASH
197 and micro-beam therapy, which require further extensive study both in-vitro and in appropriate in-vivo
198 models.

199   The LhARA consortium has conceived LhARA, the Laser-hybrid Accelerator for Radiobiological
200 Applications, as the highly flexible source delivering the temporal, spectral, and spatial beam structures that
201 are required to elucidate the mechanisms that underlie the FLASH and micro-beam effects. LhARA will
202 also allow the exploration of the vast "terra incognita" of the mechanisms by which the biological response
203 to ionising radiation is modulated by the physical characteristics of the beam. These comprehensive studies
204 are not currently possible at clinical RT facilities. Thus the LhARA facility will provide greater accessibility
205 to stable ion beams, enable different temporal fractionation schemes, and deliver reliable and reproducible
206 biological data with fewer constraints than at current clinical centres. The availability of several ion beams
207 (from protons to heavier ions) within the same facility will provide further flexibility and the ability
208 to perform direct radiobiological comparisons of the effect of different charged particles. In addition,
209 LhARA will enable exhaustive evaluations of RBE using more complex end-points (e.g. angiogenesis
210 and inflammation) in addition to routine survival measurements. The ability to evaluate charged particles
211 in conjunction with other therapies (immunotherapy and chemotherapy), and of performing in-vivo
212 experiments with the appropriate animal models is a huge advantage given the current lack of evidence in
213 these areas. LhARA therefore has the potential to yield the accumulation of radiobiological data that can
214 drive a signficant change in current clinical practice. The simulations of LhARA that are described in this
215 document have been used to estimate the dose delivered as a function of energy for protons and carbon
216 ions. Details of the simulations can be found in sections 3.3 and 3.4. The simulations show instantaneous
217 particle rates on the order of 10^9 particles per shot can be achieved, corresponding to average dose rates
218 up to $\gtrsim 400$ Gy/s for protons and $\gtrsim 10^4$ Gy/s for carbon ions. These estimates are based on the baseline
219 specifications for LhARA.

220 **Laser-hybrid beams for radiobiology and clinical application**
221 High-power lasers have been proposed as an alternative to conventional proton and carbon-ion facilities
222 for radiotherapy [Bulanov et al. (2002); Fourkal et al. (2003); Malka et al. (2004)]. The capability of

laser-driven ion beams to generate protons and high-LET carbon ions at FLASH dose rates is a significant step forward for the provision of local tumour control whilst sparing normal tissue. High-power lasers have also been proposed to serve as the basis of electron, proton and ion-beams for radiobiology [Kraft et al. (2010a); Fiorini et al. (2011); Doria et al. (2012a); Zeil et al. (2013a); Masood et al. (2014); Zlobinskaya et al. (2014)]. More recent projects (e.g. A-SAIL [A-SAIL Project (2020)], ELI [Cirrone et al. (2013)] and SCAPA [Wiggins et al. (2019)]) will also investigate radiobiological effects using laser-driven ion beams. These studies will also address various technological issues [Manti et al. (2017a); Romano et al. (2016); Masood et al. (2017); Chaudhary et al. (2017); Margarone et al. (2018)].

The LhARA collaboration's concept is to exploit a laser to drive the creation of a large flux of protons or light ions which are captured and formed into a beam by strong-focusing plasma lenses. The laser-driven source allows protons and ions to be captured at energies significantly above those that pertain in conventional facilities, thus evading the current space-charge limit on the instantaneous dose rate that can be delivered. Rapid acceleration will be performed using a fixed-field alternating-gradient accelerator (FFA) thereby preserving the unique flexibility in the time, energy, and spatial structure of the beam afforded by the laser-driven source. Modern lasers are capable of delivering a Joule of energy in pulses that are tens of femtoseconds in length at repetition rates of $\gtrsim 10 \, \text{Hz}$. At source, a laser-driven electron beam is reproducibly-well collimated and has a modest ($\sim 5\%$) energy spread. By contrast, laser-driven proton and ion sources create beams that are highly divergent, have a large energy spread, and an intensity that varies by up to 40% pulse-to-pulse. Multiple ion species, from proton to carbon, can be produced from a single laser by varying the target foil and particle capture optics. The realisation of LhARA requires each of these issues to be addressed. The LhARA consortium's vision is that LhARA will prove the principal of the novel technologies required for the development of future therapy facilities. The legacy of the LhARA programme will therefore be:

- A unique facility dedicated to the development of a deep understanding of the radiobiology of proton and ion beams; and
- The demonstration in operation of technologies that will allow particle beam therapy to be delivered in completely new regimes.

3 THE LHARA FACILITY

The LhARA facility, shown schematically in figure 1, has been designed to serve two end stations for in-vitro radiobiology and one end station for in-vivo studies. The principle components of the LhARA accelerator are: the laser-driven proton and ion source; the matching and energy selection section; beam delivery to the low-energy in-vitro end station; the low-energy abort line; the injection line for the fixed-field alternating-gradient accelerator (FFA); the FFA; the extraction line; the high-energy abort line; beam delivery to the high-energy in-vitro end station; and the transfer line to the in-vivo end station. Proton beams with energies of between 12 MeV and 15 MeV will be delivered directly from the laser-driven source to the low-energy in-vitro end station via a transfer line. The high-energy in-vitro end station and the in-vivo end station will be served by proton beams with energy between 15 MeV and 127 MeV and by ion beams (including C^{6+}) with energies up to 33.4 MeV/u. This configuration makes it natural to propose that LhARA be constructed in two stages; Stage 1 providing beam to the low-energy in-vivo end station and Stage 2 delivering the full functionality of the facility. The development of LhARA Stage 1 will include machine performance and optimisation studies designed to allow in-vitro experiments to begin as soon as possible.
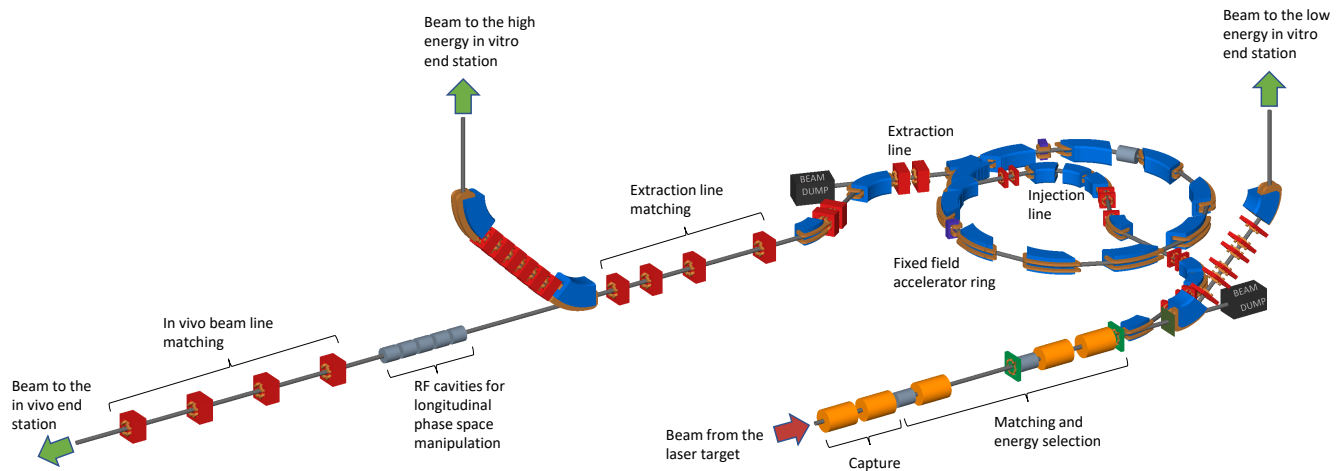
Figure 1. Schematic diagram of the LhARA beam lines. The particle flux from the laser-driven source is shown by the red arrow. The 'Capture' section is followed by the 'Matching and energy selection' section. The beam is then directed either into the $90°$ bend that takes it to the low-energy in-vitro end station, towards the FFA injection line, or to the low-energy beam dump. Post acceleration is performed using the 'Fixed field accelerator ring' on extraction from which the beam is directed either to the high-energy in-vitro end station, the in-vivo end station, or the high-energy beam dump.

265   The design parameters for the various components of LhARA are given in tables 1 and 2. The design of
266   the LhARA facility is described in the sections that follow.
267

3.1   Laser-driven proton and ion source

269   Laser-driven ions have been posited as a source for radiobiological studies for a number of years [Kraft
270   et al. (2010b); Yogo et al. (2011); Bin et al. (2012)]. Until now, the achievable ion energies, energy
271   spreads, and reproducibility of such beams have meant that such sources are not suitable for a full
272   radiobiological laboratory setting. While a number of cell irradiation experiments have been conducted
273   with laser-accelerated ions [Doria et al. (2012b); Zeil et al. (2013b); Pommarel et al. (2017); Manti et al.
274   (2017b)], these have been limited in scope to a single-shot configuration. In addition, most of these
275   experiments have been performed on high-power laser facilities with rapidly shifting priorities, where the
276   time to install dedicated diagnostic systems has not been available. At present, a dedicated ion beam for
277   radiobiology, based on a laser-driven source, is not available anywhere in the world. Therefore, LhARA
278   will be a unique, state-of-the-art system, able to explore the radiobiological benefits of a laser-accelerated
279   ion source.

280   Conventional ion sources are capable of producing ions with energies of the order of $50\,\mathrm{keV}$ with relatively
281   modest currents (of the order of $100\,\mu A$) [Osmic et al. (2012)]. A novel solution to the ion-acceleration
282   problem is to use a compact, flexible laser-driven source coupled to a state-of-the-art beam-transport line.
283   This allows an accelerating gradient of $\gtrsim 10\,\mathrm{GV/m}$ to be exploited at the laser-driven source. We propose
284   to operate in a laser-driven sheath-acceleration regime [Clark et al. (2000); Snavely et al. (2000); Daido
285   et al. (2012)] for ion generation. An intense, short laser pulse will be focused onto a target. The intense
286   electric field generated on the front surface of the target accelerates the surface electrons, driving them into
287   the material. Electrons which gain sufficient energy traverse the target, ionising the material as they go. A
288   strong space-charge electric field, the 'sheath', is created as the accelerated electrons exit the rear surface
289   of the target. This field in turn accelerates surface-contaminant ions. The sheath-acceleration scheme has

Table 1. Design parameters of the components of the LhARA facility. The parameter table is provided in a number of sections. This section contains parameters for the Laser-driven proton and ion source, the Proton and ion capture section, and the Stage 1 beam transport section.

Parameter	Value or range	Unit
Laser driven proton and ion source		
Laser power	100	TW
Laser Energy	2.5	J
Laser pulse length	25	fs
Laser rep. rate	10	Hz
Proton energy	15	MeV
Proton and ion capture		
Beam divergence to be captured	50	mrad
Gabor lens effective length	0.857	m
Gabor lens length (end-flange to end-flange)	1.157	m
Gabor lens cathode radius	0.0365	m
Gabor lens maximum voltage	65	kV
Number of Gabor lenses	2	
Alternative technology: solenoid length	1.157	m
Alternative technology: solenoid max field strength	1.3	T
Stage 1 beam transport: matching & energy selection, beam delivery to low-energy end station		
Number of Gabor lenses	3	
Number of re–bunching cavities	2	
Number of collimators for energy selection	1	
Arc bending angle	90	Degrees
Number of bending magnets	2	
Number of quadrupoles in the arc	6	
Alternative technology: solenoid length	1.157	m
Alternative technology: solenoid max field strength (to serve the injection line to the Stage 2)	0.8 (1.4)	T

been shown to produce ion energies greater than 40 MeV/u at the highest laser intensities. The maximum proton energy (E_p) scales with laser intensity (I) as, $E_p \propto I^{\frac{1}{2}}$. The laser required to deliver a significant proton flux at 15 MeV can be compact, relatively inexpensive, and is commercially available.

The distribution of proton and ion energies observed in laser-driven beams exhibits a sharp cut off at the maximum energy and, historically, the flux of laser-accelerated ion beams has varied significantly shot-to-shot. To reduce the impact of the shot-to-shot variations the choice has been made to select particles from the plateau of the two-temperature energy spectrum of the laser-accelerated ion beam. This choice should enhance ion-beam stability and allow reproducible measurements to be carried out at ultra-high dose rate using a small number of fractions. To create the flux required in the plateau region it is proposed that a 100 TW laser system is used. A number of commercial lasers are available that are capable of delivering > 2.5 J in pulses of duration < 25 fs, at 10 Hz with contrast better than $10^{10} : 1$. Shot-to-shot stability of $< 1\%$ is promised, an important feature for stable ion-beam production.

Key to the operation of this configuration is a system that refreshes the target material at high-repetition rate in a reproducible manner. A number of schemes have been proposed for such studies, from high-pressure gases [REF], cryogenic hydrogen ribbons [Margarone et al. (2016); Gauthier et al. (2017); Obst et al. (2017)], liquid sheets [Morrison et al. (2018)] and tape drives [Noaman-ul Haq et al. (2017)]. For the LhARA facility, a tape drive based on the system developed at Imperial College London is proposed. This

Table 2. Design parameters of the components of the LhARA facility. The parameter table is provided in a number of sections. This section contains parameters for the Stage 2 beam transport and the In-vitro and In-vivo end stations.

Parameter	Value or range	Unit
Stage 2 beam transport: FFA, transfer line, beam delivery to high-energy end stations		
Number of bending magnets in the injection line	7	
Number of quadrupoles in the injection line	10	
FFA: Machine type	single spiral scaling FFA	
FFA: Extraction energy	15–127	MeV
FFA: Number of cells	10	
FFA: Orbit R_{min}	2.92	m
FFA: Orbit R_{max}	3.48	m
FFA: Orbit excursion	0.56	m
FFA: External R	4	m
FFA: Number of RF cavities	2	
FFA: RF frequency	1.46–6.48	MHz
FFA: harmonic number	1, 2 or 4	
FFA: RF voltage (for 2 cavities)	8	kV
FFA: spiral angle	48.7	Degrees
FFA: Max B field	1.4	T
FFA: k	5.33	
FFA: Magnet packing factor	0.34	
FFA: Magnet opening angle	12.24	degrees
FFA: Magnet gap	0.047	m
FFA: Ring tune (x,y)	(2.83,1.22)	
FFA: γ_T	2.516	
FFA: Number of kickers	2	
FFA: Number of septa	2	
Number of bending magnets in the extraction line	2	
Number of quadrupoles in the extraction line	8	
Vertical arc bending angle	90	Degrees
Number of bending magnets in the vertical arc	2	
Number of quadrupoles in the vertical arc	6	
Number of cavities for longitudinal phase space manipulation	5	
Number of quadrupoles in the in vivo beam line	4	
In-vitro biological end stations		
Maximum input beam diameter	1-3	cm
Input beam energy spread	< 2	%
Input beam uniformity	< 5	%
Scintillating fibre layer thickness	0.25	mm
Air gap length	5	mm
Cell culture plate thickness	1.3	mm
Cell layer thickness	0.03	mm
Number of end stations	2	
In-vivo biological end station		
Maximum input beam diameter	1-3	cm
Input beam energy spread	< 2	%
Input beam uniformity	< 5	%
Beam options	Spot-scanning, passive scattering, micro-beam	

307 system is capable of reliable operation at target thicknesses down to 5 μm, using both aluminium and steel
308 foils, and down to 18 μm using plastic tapes. Such tape-drive targets allow operation at high charge (up to
309 100 pC at 15 ± 1 MeV, i.e. $> 10^9$ protons per shot) and of delivering high-quality proton and ion fluxes at
310 repetition rates of up to 10 Hz or greater.

311 The unique features of the laser-driven ion source proposed for LhARA offer a number of opportunities
312 to push the frontiers in the fields of sustained high-frequency ion generation, advanced targetry solutions
313 and active, high-repetition rate diagnostics. The successful development and execution of LhARA will
314 provide a leap forward in terms of capability and open up exciting new opportunities for applications not
315 just in radiobiology, but also medical isotope production and materials processing. While pushing these
316 new frontiers, the radiobiological-capabilities of LhARA are based on relatively low-energy ion beams,
317 mitigating the risks that operating at the energy-frontier of the field would imply.

318 High repetition-rate operation of laser-driven radiation sources is a relatively new, but active area of
319 interest [Noaman-ul Haq et al. (2017); Aurand et al. (2019); Streeter et al. (2018); Dann et al. (2019);
320 Kirschner et al. (2019)]. Such operating schemes pose a number of engineering challenges. It is proposed
321 to apply machine-learning and genetic algorithms to the optimisation of the laser-target interaction to
322 optimise the beam charge, peak energy, energy spread, and divergence of the ion flux produced [Aurand
323 et al. (2019)]. These techniques will require appropriate R&D effort. The first experiments of this kind will
324 be possible using the existing laser capabilities at Imperial College London, the Central Laser Facility at
325 the Rutherford Appleton Laboratory, and elsewhere.

326 The careful control of the tension on the tape in a tape-drive target is critical for reproducible operation.
327 The tape must be stretched to flatten the surface, without stretching it to its plastic response. Surface
328 flatness is important for a number of reasons. Rippling of the front surface modifies the laser absorption
329 dramatically; uncharacterised rippling can make shot-to-shot variations significant and unpredictable
330 [Noaman-ul Haq et al. (2017)]. Similarly, rear surface perturbations can modify the sheath field, resulting
331 in spatial non-uniformities of the proton beam or suppression of the achievable peak energies. Tape drives
332 with torsion control and monitoring to maintain a high-quality tape surface have been designed and operated
333 in experiments at Imperial College London. The development of these targets continues with a view to the
334 development of new, thinner tapes for improved ion generation and the creation of ion species other than
335 proton and carbon. This is an active area of R&D that will continue with the development of LhARA.

336 High repetition-rate ion-beam diagnostics will also need to be developed to allow successful execution
337 of LhARA. Such diagnostics will need to measure both the energy spectrum and the spatial profile of
338 the beams. Current methods are destructive and are often limited to low-repetition rate. Passive detectors
339 have not been demonstrated in the conditions that will pertain at LhARA. Technologies being evaluated to
340 address the issues raised by ion-source diagnostics for LhARA are discussed in section 3.5.
341

3.2 Proton and ion capture

343 The use of an electron cloud as a focusing element for charged-particle beams was first proposed by
344 Gabor in 1947 [Gabor (1947)] who noted that a cloud of electrons uniformly distributed about the axis of a
345 cylindrical vessel would produce an ideal focusing force on a beam of positively charged particles. The
346 focal length of such a lens scales with the energy of the incoming particle beam allowing such lenses to
347 provide strong focussing of high-energy beams. Confinement conditions in the radial and axial directions
348 can be determined [Pozimski and Aslaninejad (2013)]. In the radial direction, where there is magnetic
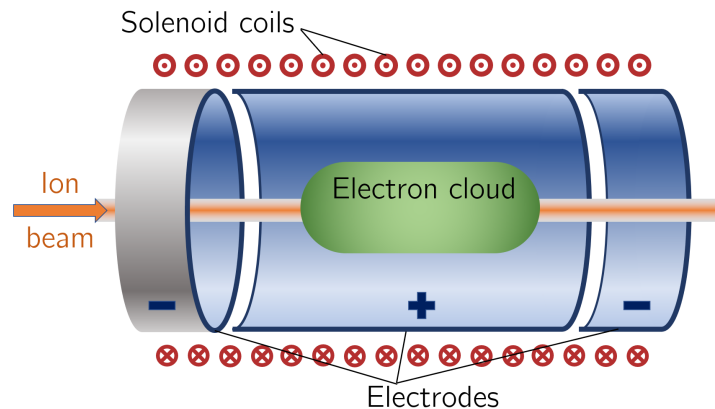
Figure 2. Schematic diagram of a Penning-Malmberg trap of the type proposed for use in the Gabor lenses to be used in LhARA. The solenoid coils, and the direction of current flow, are indicated by the red circles. The confining electrostatic potential is provided using a central cylindrical anode and two cylindrical negative end electrodes. The ion beam enters on-axis from the left and the electron cloud is indicated by the green shaded area.

349   confinement and Brillouin flow, the number density of electrons, n_e, that can be contained is given by:

$$n_e = \frac{\epsilon_0 B^2}{2 m_e e} \, ; \tag{1}$$

350   where B is the magnetic field, e the magnitude of the charge on the electron, m_e the mass of the electron,
351   and ϵ_0 the permittivity of free space. In the longitudinal direction there is electrostatic confinement for
352   which n_e is given by:

$$n_e = \frac{4 \epsilon_0 V_A}{e R^2} \, ; \tag{2}$$

353   where R is the radius of the cylindrical anode which is held at the positive potential V_A. For the electron
354   densities of interest for LhARA the required anode voltage is of the order of $50\,\text{kV}$.

355   In the thin lens approximation, the focal length, f, of a Gabor lens can be expressed in terms of the
356   magnetic field and the particle velocity, v_p [Reiser (1989)]:

$$\frac{1}{f} = \frac{e^2 B^2}{4 m_e m_p v_p^2} l \, ; \tag{3}$$

357   where m_p is the mass of the particles in the beam. The focal length of the Gabor lens is therefore
358   proportional to the kinetic energy or, equivalently, the square of the momentum, of the incoming beam. By
359   comparison, the focal length for a solenoid is proportional to the square of the momentum and that of a
360   quadrupole is proportional to momentum. At the particle energies relevant to LhARA, the Gabor lens or
361   solenoid are therefore preferred.

362   For a given focal length, the magnetic field required in the Gabor lens is reduced compared to that of a
363   solenoid that would give equivalent focusing [Pozimski and Aslaninejad (2013)]:

$$B_{GPL} = B_{sol} \sqrt{Z \frac{m_e}{m_{ion}}} \, ; \tag{4}$$

364 where B_{GPL} and B_{sol} are the magnetic fields in the Gabor lens and the equivalent solenoid respectively;
365 m_{ion} is the mass of the ions being focused, and Z is the charge state of the ions. In the case of a proton beam
366 the reduction factor is 43. Thus, for example, where a 2 T superconducting solenoid would be required, the
367 magnetic field required for a Gabor lens would only be 47 mT. This means the cost of the solenoid for a
368 Gabor lens can be significantly lower than the cost for a solenoid of equivalent focusing strength.

369 An expression for the focal length as a function of electron number density can be derived by substituting
370 equation (1) into equation (3) to give:

$$\frac{1}{f} = \frac{e^3 n_e}{2\epsilon_0 U} l \,; \tag{5}$$

371 where $U = m_p v_p^2$ is the energy of the particle beam. The focal length of the Gabor lens is inversely
372 proportional to the number density of electrons trapped in the cloud. The focal lengths desired to capture
373 the proton and ion beams at LhARA have been chosen such that the required electron number densities are
374 conservative and lie within the range covered in published experiments.

375 Instability of the electron cloud is a concern in the experimental operation of Gabor lens; azimuthal
376 beam disruption due to the diocotron instability has been seen in both experiment and theory [Meusel et al.
377 (2013)]. Theory indicates that the diocotron instability is most problematic under well-defined geometric
378 conditions. The reliable operation of a Gabor lens in a regime free from this instability has yet to be
379 demonstrated. Gabor lenses promise very strong focusing, simple construction, and low magnetic field,
380 all attractive features for LhARA. However, these attractive features come at the cost of relatively high
381 voltage operation ($\gtrsim 50$ kV) and possible vulnerability to instability.

382 With reliable operation of Gabor lenses as yet unproven we plan a two-part experimental and theoretical
383 programme of research to prove Gabor-lens suitability. Initial work will include: theoretical investigation
384 of lens stability in a full 3D particle-in-cell code such as VSIM [VSI (2020)]; and the development of
385 electron-density diagnostics based on interferometric measurement of the refractive-index change. These
386 activities will be applied to a time-invariant electron cloud. A test Gabor lens will be constructed to allow
387 validation of both the simulation results and a new diagnostic using an alpha emitter as a proxy for the
388 LhARA beam. In addition, the initial investigation will include the design of an electron beam to fill the
389 lens. This last objective will enable the second part of the experimental project; the operation of the Gabor
390 lens in short pulses. It is attractive to match the timing of the establishment of the electron cloud within the
391 Gabor lens to that of the beam and thereby limit instability growth. The research project is time limited
392 such that, should it not prove possible to produce a suitable Gabor lens, there remains time to procure
393 conventional solenoids in their place.

394

395 ### 3.3 Beam transport and delivery to the low-energy in-vitro end station

396 Beam-transport from the laser-driven ion source and delivery to the low-energy in-vivo end station is
397 required to deliver a uniform dose distribution at the cell layer. Beam losses must be minimised for radiation
398 safety and to maximise the dose that can be delivered in a single shot. The transport line has been designed
399 to minimise regions in which the beam is brought to a focus to reduce the impact of space-charge forces on
400 the beam phase-space. An optical solution was initially developed using Beamoptics [Autin et al. (1998)]
401 and MADX [Grote and Schmidt (2003)]. Accurate estimation of the performance of the beam line requires
402 the inclusion of space-charge forces and particle-matter interactions. Therefore, performance estimation
403 was performed using Monte Carlo particle-tracking from the ion source to the end station. BDSIM [Nevay
404 et al. (2020)], which is based on the Geant4 toolkit was used for the simulation of energy deposition arising
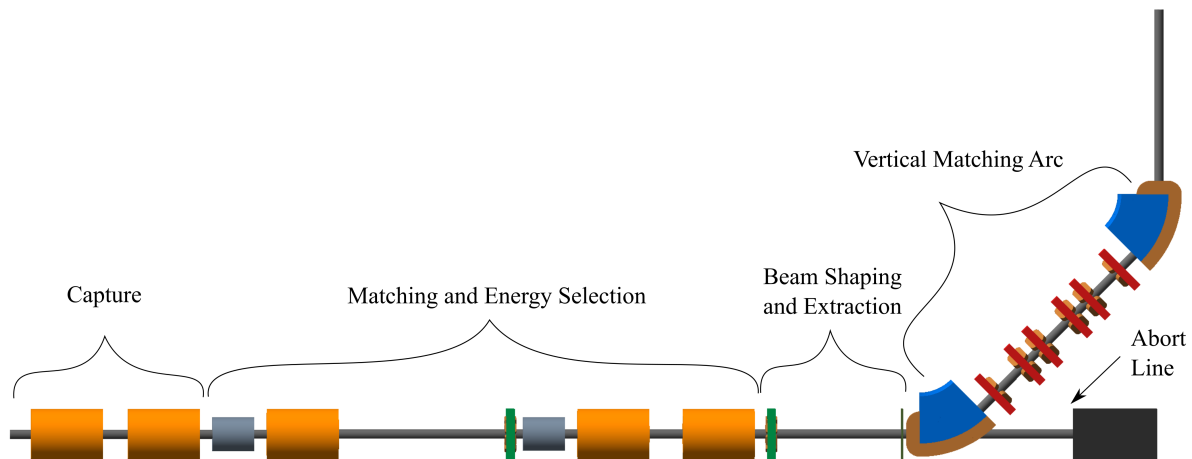
Figure 3. Beam transport for Stage 1 of LhARA visualised in BDSIM, showing five machine sections. The capture section is composed of two Gabor lenses (orange cylinders). The matching and energy selection section includes three Gabor lenses, two RF cavities (grey cylinders) and an octupole magnet (green disc). The beam shaping and extraction section includes a second octupole and a collimator (black vertical bar). The vertical matching arc directs the beam into the low-energy in-vitro end station and is composed of two $45°$ dipoles and six quadrupoles. The total length of this beam line is 17.255 m.

405 from beam interactions with the material in the accelerator and the end station and GPT [De Loos and
406 Van der Geer (1996)] was used for evaluating the full 3D impact of space-charge.

407   An idealised Gaussian beam was generated with a spot size of $4\,\mu$m FWHM, an angular divergence of
408 50 mrad, 35 fs FWHM bunch length, and an energy spread of 1×10^{-6} MeV. The maximum estimated
409 bunch charge is 1×10^{9} protons. The presence of a substantial electron flux produced from the laser target
410 compensates the high proton charge density in the vicinity of the ion-production point. Therefore, the first
411 5 cm of beam propagation was simulated without space-charge. Beyond this, the proton beam will have
412 separated from the lower energy electrons sufficiently for space-charge to become a prominent effect and
413 cause an emittance growth. Therefore, a further 5 cm drift was simulated including space-charge forces. At
414 a distance of 10 cm from the ion source the beam is at the exit of the laser-target vessel. The kinematic
415 distributions of ions in the beam were stored at this point and passed to the relevant BDSIM and GPT
416 simulations of the downstream beam line.

417   The beam line, shown schematically in figure 3, is composed of five sections: beam capture; matching
418 and energy selection; beam shaping; vertical arc matching; and an abort line. The capture section uses two
419 Gabor lenses to minimise the beam's transverse momentum. Beyond the capture section, an RF cavity
420 permits control of the bunch length and manipulation of the longitudinal phase-space. A third Gabor lens
421 then focuses the bunch to a small spot size after which a second RF cavity is located to provide further
422 longitudinal phase-space manipulation. Two further Gabor lenses bring the beam parallel once more in
423 preparation for the vertical $90°$ arc. All Gabor lenses have an inner radius of 3.65 cm and an effective length
424 of 0.857 m. All lenses operate below the maximum cathode voltage of 65 kV.

425   A parallel beam emerges from the final Gabor lens, providing significant flexibility for the inclusion of
426 beam shaping and extraction systems. Beam uniformity will be achieved using octupole magnets to provide
427 third-order focusing to perturb the first-order focusing from the Gabor lenses. Such schemes have been
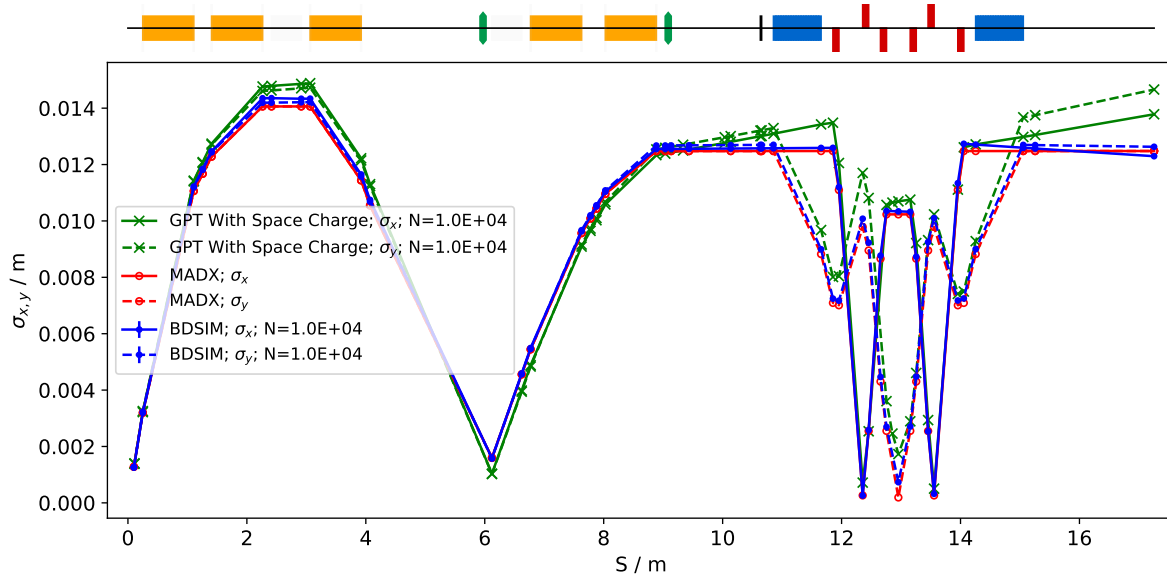428 demonstrated in a number of facilities [Tsoupas et al. (1991); Urakabe et al. (1999); Amin et al. (2018)].

Figure 4. Horizontal (solid lines) and vertical (dashed lines) beam sizes through the in-vitro beam transport, simulated with space-charge in GPT (green), and without space-charge in MADX (red) and BDSIM (blue).

429 A suitable position for the first octupole was identified to be after the final Gabor lens where the beam
430 is large; its effect on the beam is expected to be significant. Octupoles were only modelled in BDSIM
431 simulations as GPT does not have a standard component with an octupolar field. The typical rectangular
432 transverse distribution resulting from octupolar focusing requires collimation to match the end station's
433 circular aperture. A collimator is therefore positioned at the start of the vertical arc. Further simulations are
434 required to determine the optimum position of the second octupole and to evaluate the performance of the
435 octupoles. The switching dipole which directs the beam to the injection line of the FFA in Stage 2 will
436 be located between the second octupole and the collimator, requiring the octupole to be ramped down for
437 Stage 2 operation.

438   The vertical arc uses transparent optics in an achromat matching section to ensure that the first-order
439 transfer map through the arc is equivalent to the identity transformation and that any dispersive effects are
440 cancelled. A 2 m drift tube is added after the arc to penetrate the concrete shielding of the end station floor
441 and to bring the beam to bench height. The abort line consists of a drift followed by a beam dump and
442 requires the first vertical dipole to ramp down, preventing charged-particle transportation to the end station.

443   The underlying physics of plasma-lens operation cannot be simulated in BDSIM or GPT, however it
444 can be approximated using solenoid magnets of equivalent strength. RF cavity fields were not simulated.
445 10000 particles were simulated corresponding to the estimated maximum bunch charge of 1×10^9 protons.
446 Figure 4 shows excellent agreement between horizontal and vertical transverse beam sizes in BDSIM
447 and MADX, verifying the beam line's performance in the absence of space-charge effects. Reasonable
448 agreement between BDSIM and GPT is also seen when space-charge forces are included in GPT. Emittance
449 growth is observed prior to the first solenoid, affecting the optical parameters throughout the machine.
450 However, the resulting beam dimensions at the cell layer of 1.538 cm horizontally and 1.205 cm vertically
451 are not significantly different from the ideal beam in BDSIM. Further adjustments of the Gabor lenses
452 and arc-quadrupole strengths may compensate for this. The transmission efficiency of the beam line is
453 approximately 100%.

454   The small bunch dimensions in both transverse planes at the focus after the third Gabor lens, where
455 the energy selection collimator will be placed, remains a concern if the effect of space-charge has been
456 underestimated. Similar bunch dimensions are achieved in the vertical arc, however, quadrupolar focusing
457 is confined to a single plane mitigating further emittance growth. Further tuning of the Gabor lens voltages
458 in the capture section may compensate space-charge effects, reducing the non-zero transverse momentum
459 seen entering the vertical arc.

460   To investigate beam uniformity, BDSIM simulations with and without octupoles and collimation for beam
461 shaping were conducted. Both octupoles were arbitrarily set to a strength of $K3 = 6000$ with a magnetic
462 length of 0.1 m and pole tip radius of 5 cm, which, for a 15 MeV beam corresponds to pole tip field of
463 0.42 T. A 2 cm thick iron collimator with a 40 mm diameter aperture was positioned 1.5 m downstream
464 of the octupole. Figure 5 shows the beam phase-space and particle distributions at the end station for the
465 transverse and longitudinal axes with and without beam shaping. Without octupoles the spatial profile
466 is Gaussian as expected, however, beam uniformity is improved with octupoles and collimation. The
467 total beam width is 3.58 cm horizontally and 3.46 cm vertically which is sufficient to irradiate one well
468 in a six-well cell-culture plate. Further optimisation is required to improve uniformity whilst optimising
469 beam-line transmission, which is approximately 70% for the results presented in figure 5. An aberration
470 can be seen in both transverse planes with and without beam shaping; this effect originates upstream of
471 the octupoles in the solenoids, and persists through to the end station. These aberrations are a concern,
472 however, future simulation efforts will replace the solenoids with a full electromagnetic simulation of the
473 Gabor lens. This change is likely to change the aberrations. The non-Gaussian energy distribution without
474 beam shaping is a result of space-charge forces at the ion source; the distribution persists to the end station
475 as no components which affect the longitudinal phase space were simulated. The Gaussian distribution
476 seen with beam shaping is due to collimation.

477   The proposed design is capable of delivering beams of the desired size to the in-vitro end station. Space-
478 charge effects impact the beam transport performance but it is believed that this can be mitigated with
479 minor adjustments to the Gabor lenses in the capture section. Initial studies indicate that a uniform beam
480 can be delivered with further optimisation of the octupoles and collimator.

481
482 ### 3.3.1 Alternative Design

483   To mitigate potential emittance growth from space-charge forces, an alternative beam line design was
484 developed in which the final two Gabor lenses in the matching and energy selection section are replaced by
485 four quadrupoles, limiting any bunch focusing to one plane at a time. The resulting machine is reduced
486 in length to 15.439 m. Without space-charge effects, a bunch size of 2.5 mm at the end station can be
487 achieved. With space-charge, the initial emittance growth prior to the first solenoid is once again observed
488 leading to an increased beam size at the entrance of the first quadrupole, resulting in a spatially asymmetric
489 and divergent beam at the end station. It is believed that the space-charge effects can be compensated
490 by applying the same Gabor-lens optimisation as in the baseline design in addition to adjustments of the
491 alternative design's quadrupoles settings, and that beam parameters similar to those without space-charge
492 may be recovered. The alternative design provides a solution that is more resilient to space-charge effects
493 than the baseline, however, only the lower bound on the desired beam size can be achieved. Further
494 optimisation is required not only to optimise optical performance but also to optimise octupole settings and
495 to determine whether a beam with the desired uniformity can be delivered to the end station.
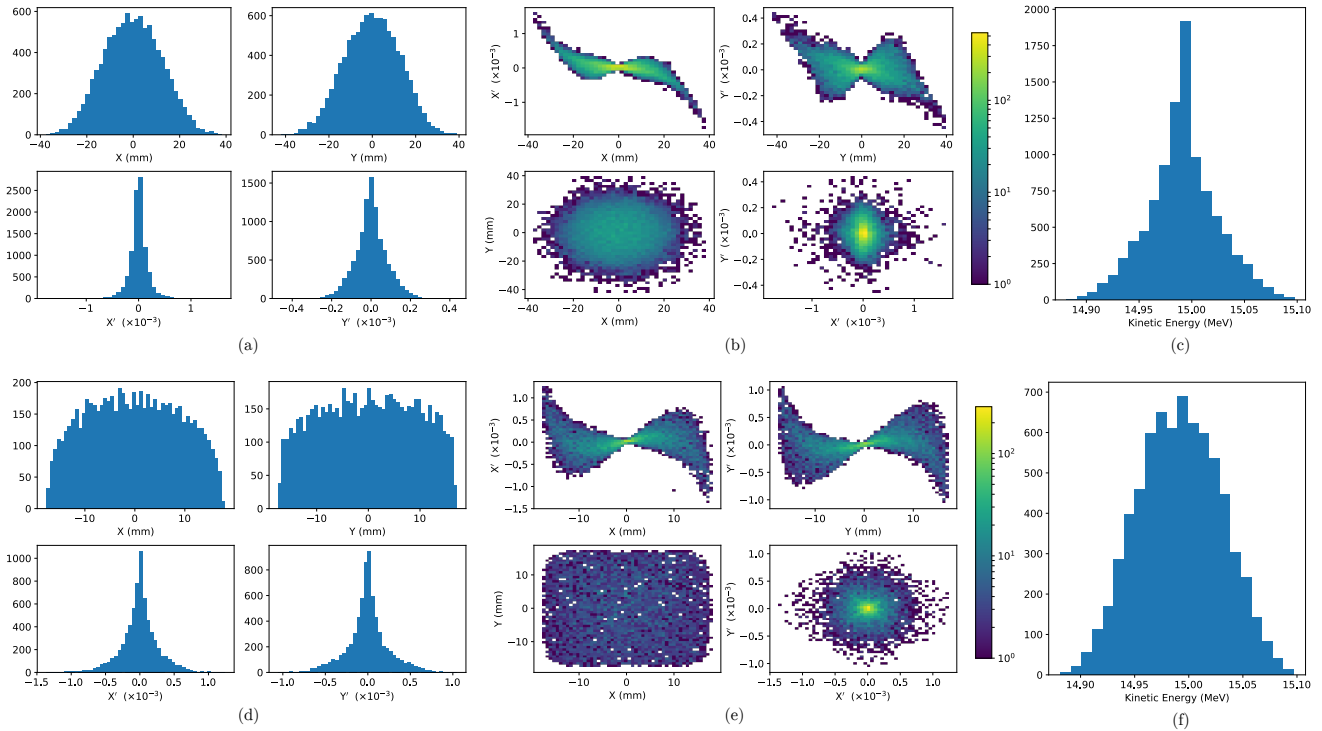
496

Figure 5. Beam phase space distributions in the transverse plane, (X, Y); X′ and Y′ give the slope relative to the Z axis. The transverse phase space is shown in figures a and b for simulations without octupolar focusing and collimation, with the kinetic energy distribution shown in c. The same phase space distributions simulated with the effect of octupoles and collimation are in figures d, e, and f.

3.4 Post-acceleration and beam delivery to the in-vitro and in-vivo end stations

A fixed-field alternating-gradient accelerator (FFA), based on the spiral scaling principle [Krest et al. (1956); Symon et al. (1956); Fourrier et al. (2008); Tanigaki et al. (2006)], will be used to accelerate the beam in LhARA Stage 2 to obtain energies greater than the 15 MeV protons and 4 MeV/u carbon (C^{6+}) ions delivered by the laser-driven source. FFAs have many advantages for both medical and radiobiological applications such as: the capability to deliver high and variable dose; rapid cycling with repetition rates ranging from 10 Hz to 100 Hz or beyond; and the ability to deliver various beam energies without the use of energy degraders. An FFA is relatively compact due to the use of combined function magnets, which lowers the overall cost compared to conventional accelerators capable of delivering beams at a variety of energies such as synchrotrons. Extraction can be both simple and efficient, with the possibility for multiple extraction ports to be used. Furthermore, FFAs can accelerate multiple ion species, which is very important for radiobiological experiments and typically very difficult to achieve with cyclotrons.

A typical FFA is able to increase the beam momentum by a factor of three, though a greater factor may be achieved. For LhARA, this translates to a maximum proton-beam energy of 127 MeV from an injected beam of 15 MeV. For carbon ions (C^{6+}) with the same rigidity, a maximum energy of approximately 33.4 MeV/u can be produced.

The energy at injection into the FFA determines the beam energy at extraction. The injection energy will be changed by varying the focusing strengths in the Stage 1 beam line from the capture section through to the extraction line and the FFA ring. This will allow the appropriate energy slice from the broad energy spectrum produced at the laser-driven source to be captured and transported to the FFA. The FFA will then
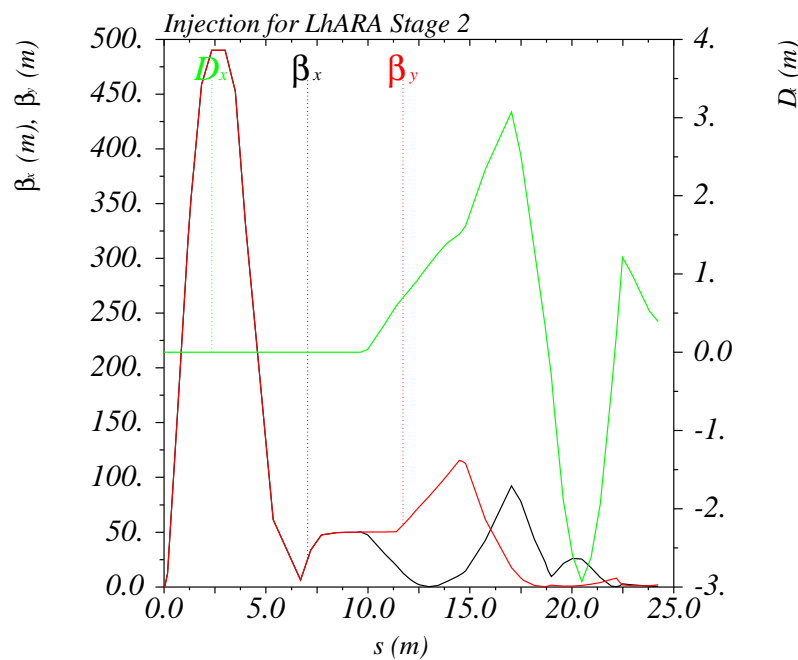

Figure 6. Twiss β_x and β_y functions and dispersion in the beam line consisting of the modified Stage 1 lattice and the transfer line allowing injection of the beam into the FFA ring. S goes from the laser target to the exit of the injection septum.

accelerate the beam, acting as a three-fold momentum multiplier. This scheme simplifies the injection and extraction systems since their geometry and location can be kept constant.

A second, 'high-energy', in-vitro end station will be served by proton beams with a kinetic energy in the range 15–127 MeV and carbon-ion beams with energies up to 33.4 MeV/u. The extraction line from the FFA leads to a 90° vertical arc to send the beam to the high-energy in-vitro end station. If the first dipole of the arc is not energised, beam will be sent to the in-vivo end station. The extraction line of the FFA includes a switching dipole that will send the beam to the high-energy-beam dump if it is not energised. The detailed design of the high-energy abort line will be performed as part of the R&D programme. The design of the abort line will take into account the requirement that stray radiation from the aborted beam does not enter the end stations.

3.4.1 Injection line

The settings of the Stage 1 beam line need to be adjusted to reduce the Twiss β function propagating through the injection line to allow beam to be injected into the FFA ring. The optical parameters in the Stage 1 beam line after adjustment are shown in figure 6. The beam is diverted into the injection line by a switching dipole. The injection line transports the beam to the injection septum magnet. In the injection line matches the beam in both transverse planes and beam dispersion to the values dictated by the periodic conditions in the FFA cell (figure 6). The presence of dispersion in the injection line allows a collimator to be installed for momentum selection before injection. The beam is injected from the inside of the ring, which requires the injection line to cross one of the straight sections between the FFA magnets, see figure 7.
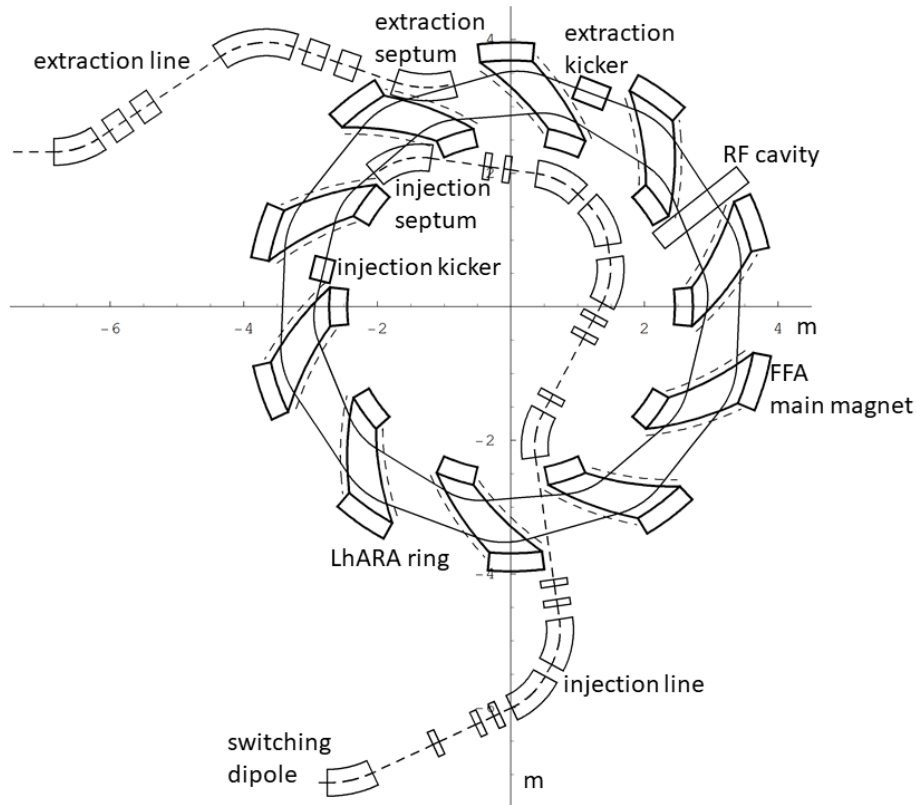
Figure 7. The layout of the injection line from the switching dipole to the injection septum together with the FFA ring, some of its subsystems and the first part of the extraction line.

3.4.2 FFA ring

The magnetic field, B_y, in the median plane of a scaling spiral FFA is given by:

$$B_y = B_0 \left[\frac{R}{R_0} \right]^k F \left(\theta - \ln \left[\frac{R}{R_0} \right] \tan \zeta \right) ; \tag{6}$$

where B_0 is the magnetic field at radius R_0, k is the field index, ζ corresponds to the spiral angle and F is the 'flutter function'. This field law defines a zero-chromaticity condition, which means the working point of the machine is independent of energy up to field errors and alignment imperfections and avoids resonance crossings that would reduce the beam quality and may lead to beam loss.

Table 2 gives the main design parameters of the FFA ring. The ring consists of ten symmetric cells each containing a single combined-function spiral magnet. The choice of the number of cells is a compromise between the size of the orbit excursion, which dictates the radial extent of the magnet, and the length of the straight sections required to accommodate the injection and extraction systems.

The betatron functions and dispersion in one lattice cell at injection are shown in figure 8a. The tune diagram, showing the position of the working point of the machine in relation to the main resonance lines, is shown in figure 8b. Tracking studies were performed using a step-wise tracking code in which the magnetic field is integrated using a Runge-Kutta algorithm [Lagrange et al. (2018)]. The magnetic field in the median plane was obtained using the ideal scaling law (equation 6) and using using Enge functions to give the fringe fields. Out of the median plane the field was obtained using a 6th-order Taylor of the field.
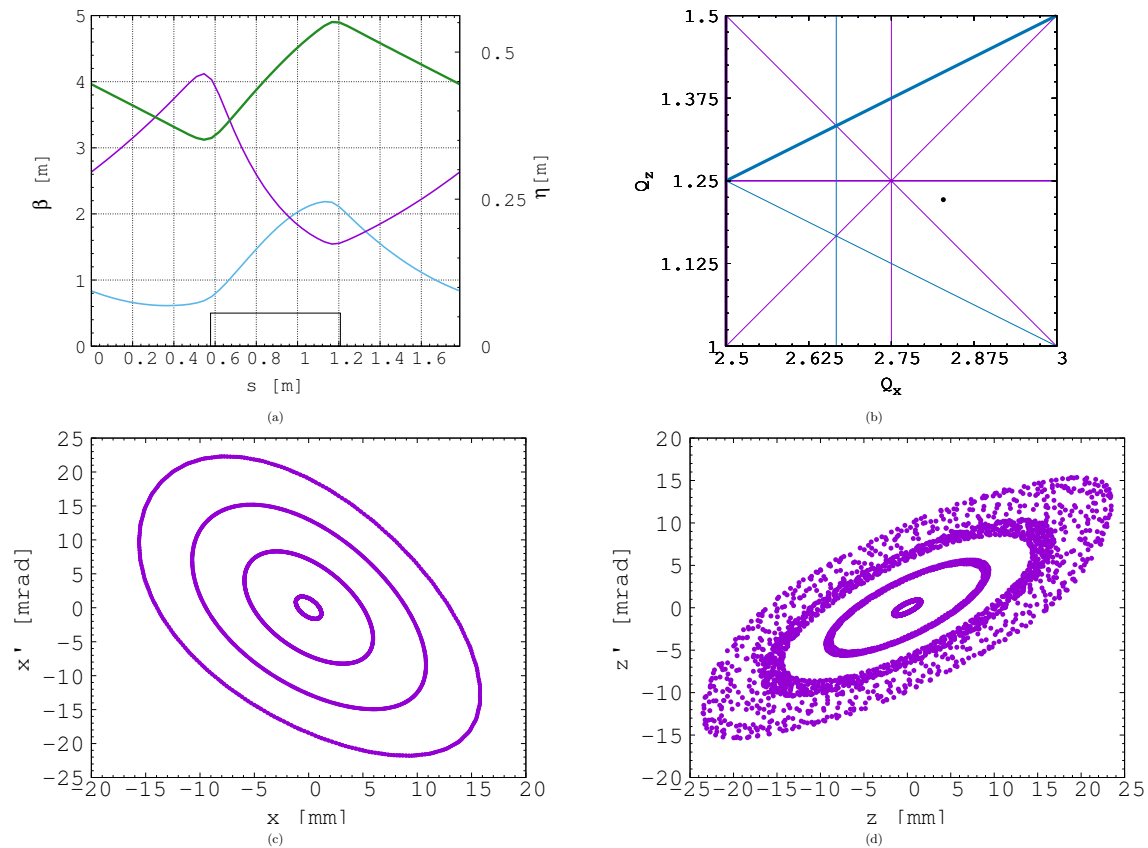
Figure 8. Beam optics and tracking in the FFA. Twiss β_h (blue), β_v (purple) functions and dispersion (green) in one lattice cell of the FFA ring (a). The working point of the FFA ring at (2.83, 1.22) on the tune diagram (b). The results of the horizontal (c) and vertical (d) dynamical acceptance study in the FFA ring, where a 1 mm offset is assumed in the vertical and horizontal planes respectively.

The dynamical acceptance for 100 turns, shown for the horizontal and vertical planes in figures 8c and 8d respectively, are significantly larger than the beam emittance, even when the most pessimistic assumption is used. These results confirm that a good machine working point has been chosen.

A full aperture, fast injection of the beam will be performed using a magnetic septum, installed on internal side of the ring, followed by a kicker magnet situated in a consecutive lattice cell, as shown in figure 7. The specifications of the injection system are dictated by the parameters of the beam at injection, which are summarised for the nominal proton beam in table 3. The beam at injection has a relatively small emittance and short bunch length, which limits the intensity accepted by the ring due to the space-charge effect. If the beam emittance is adjusted such that is larger then the nominal value by a factor of 1.7, then an intensity of approximately 10^9 protons would be accepted by the ring at the space-charge limit. Fast extraction of the beam over the full aperture will be performed using a kicker magnet followed by a magnetic septum installed in a consecutive lattice cell close to the extraction orbit.

Acceleration of the beam to 127 MeV will be done using an RF system operating at harmonic number $h = 1$ with an RF frequency range from 2.89 MHz to 6.48 MHz. The RF voltage required for 10 Hz operation corresponds to only 0.5 kV, however, with such a low voltage, the energy acceptance at injection would be limited to $\pm 0.1\%$ so a voltage of 8 kV is required to increase the energy acceptance to $\pm 0.7\%$.

Table 3. Summary of the main parameters for the proton beam at the injection to the FFA ring. These parameters correspond to the nominal (maximum) acceleration mode of operation.

Parameter	unit	value
Beam energy	MeV	15
Total relative energy spread		$\pm 0.7\%$
Nominal physical RMS emittance (both planes)	π m rad	4.1×10^{-7}
Incoherent space charge tune shift		-0.2
Bunching factor		0.05
Total bunch length	ns	17.5
Beam intensity		5.7×10^8

570 This voltage can be achieved with just two cavities [Yonemura et al. (2008)]. Normal conducting spiral-
571 scaling FFA magnets, similar to the ones needed for LhARA, have been constructed successfully [Tanigaki
572 et al. (2006); Planche et al. (2009)] using either distributed, individually-powered coils on a flat pole piece
573 or using a conventional gap-shaping technique. For the LhARA FFA, we a variation of the coil-dominated
574 design recently proposed at the Rutherford Appleton Laboratory in R&D studies for the upgrade of the
575 ISIS neutron and muon source. In this case, the nominal scaling field is achieved using a distribution of
576 single-powered windings on a flat pole piece. The tuning of the parameter k can be then achieved using up
577 to three additional windings that are powered independently. The extent of the fringe field across the radius
578 of the magnet must be carefully controlled using a 'field clamp' to achieve zero-chromaticity. An active
579 clamp, in which additional windings are placed around one end of the magnet, may be used to control
580 the flutter function and thereby vary independently the vertical tune of the FFA ring. Since the magnetic
581 field of the FFA ring needs to be adjusted to provide variable-energy operation, a laminated design may
582 be required to reduce the time required to change the field. The magnet gap of 4.7 cm given in table 2 is
583 estimated assuming the flat-pole design of the magnet. The details of the design will be addressed in as
584 part of the LhARA R&D programme.

585
586 ### 3.4.3 Extraction Line

587 Substantial margins in the beam parameters were assumed in the design of the extraction line from the
588 FFA due to uncertainties in the beam distributions provided beam by the Stage 1 beam transport, FFA
589 injection line, and the uncertainty introduced by the absence of space-charge effects in the simulation of
590 acceleration in the ring. Therefore, the beam emittance was allowed, pessimistically, to be as large as a
591 factor of ten greater than in the nominal value, which was derived assuming that the normalised emittance
592 is conserved from the source, through the Stage 1 beam line, and in the FFA ring. In the nominal case, the
593 physical emittance of the beam is affected by the adiabatic damping only. A substantial flexibility in the
594 optics of the extraction line is required as extraction line must accommodate a wide spectrum of beam
595 conditions to serve the in-vitro and in-vivo end-stations

596 Detailed studies were carried out for proton beams with kinetic energies of 40 MeV and 127 MeV. Table
597 4 gives the Twiss β values for different beam sizes for the 40 MeV and 127 MeV proton-beam scenarios
598 assuming a Gaussian beam distribution. The optics and geometric acceptance of the system is approximately
599 the same for the 40 MeV and 127 MeV beams. This justified the working hypothesis that beam emittance is
600 approximately the same for both beam energies. This assumption will be revised as soon as space-charge
601 simulations for the entire system are available.

Table 4. Beam emittance values and target β values for different beam sizes for 40 MeV and 127 MeV beams. The beam size is taken to be four times the sigma of the transverse beam distribution.

	40 MeV protons (Nominal)	127 MeV protons (Nominal)	127 MeV protons (Pessimistic)
RMS Emittance (ϵ_x, ϵ_y) [π mm mrad]	0.137	0.137	1.37
β [m] for a 1 mm spot size	0.46	0.46	0.039
β [m] for a 10 mm spot size	46	46	4.5
β [m] for a 30 mm spot size	410	410	40

602   The first two dipoles and four quadrupoles of the extraction line bend the beam coming from the extraction
603 septum of the FFA such that it is parallel to the low-energy beam line while ensuring that dispersion is
604 closed. Closing the dispersion is critical as off-momentum particles will follow trajectories different to
605 those followed by particles with the design momentum and therefore impact the size and shape of the beam
606 downstream. The second part of the extraction line consists of four quadrupoles which transport the beam
607 either to the first dipole of the vertical arc beam that serves the high-energy in-vitro end station or to the
608 in-vivo end-station, if this dipole is not energised. These quadrupoles provide the flexibility required to
609 produce the different beam sizes for the in-vitro end station as specified in table 4.

610
611 ### 3.4.4 High-energy in-vitro beam line

612   The high energy in-vitro beam line transports the beam from the exit of the extraction line and delivers
613 it to the high energy in-vitro end station. The $90°$ vertical bend is a scaled version of the low energy
614 vertical arc, following the same design principles, and also consists of two bending dipole magnets and six
615 quadrupole magnets. To accommodate the higher beam energies, the lengths of the magnets were scaled in
616 order to ensure that peak magnetic fields were below the saturation limits of normal conducting magnets.
617 The bending dipole magnet lengths were increased to 1.2 m each and the quadrupole lengths were tripled to
618 0.3 m each. The overall length of the arc then becomes 6 m, compared to 4.6 m for the low energy in-vitro
619 arc. This difference in arc length means the high-energy in-vitro arc finishes about 0.9 m higher than the
620 low-energy one. This difference can easily be accommodated by adjusting the final drift lengths.

621   The quadrupole strengths for the scaled high-energy in-vitro arc were obtained using MAD-X and
622 tracking simulations using BDSIM show good agreement, see figure 9. The input beam distribution used
623 in BDSIM was assumed to be Gaussian with Twiss $\beta = 46$, which gives a beam size of about 10 mm.
624 GPT simulations were performed which show small discrepancies due to space-charge effects. It may be
625 possible to compensate for this by adjusting the strengths of the quadrupoles in the arc and the matching
626 section in the extraction line.

627
628 ### 3.4.5 In-vivo beam line

629   If the first dipole of the high-energy in-vitro arc is not energised then beam is sent to the in-vivo end
630 station. From the end of the extraction line, 7.7 m of drift is necessary to clear the first bending dipole of
631 the in-vitro arc, to provide space for the five RF cavities needed for longitudinal phase-space manipulation
632 and to allow space for diagnostic devices. Following this drift is a further 6.6 m of beam line that includes
633 four quadrupoles, each of length 0.4 m, which are used to perform the final focusing adjustments of the
634 beam delivered to the in-vivo end station. A final 1.5 m drift at the end is reserved for scanning magnets to
635 be installed to perform spot scanning and to penetrate the shielding of the in-vivo end station. In total the
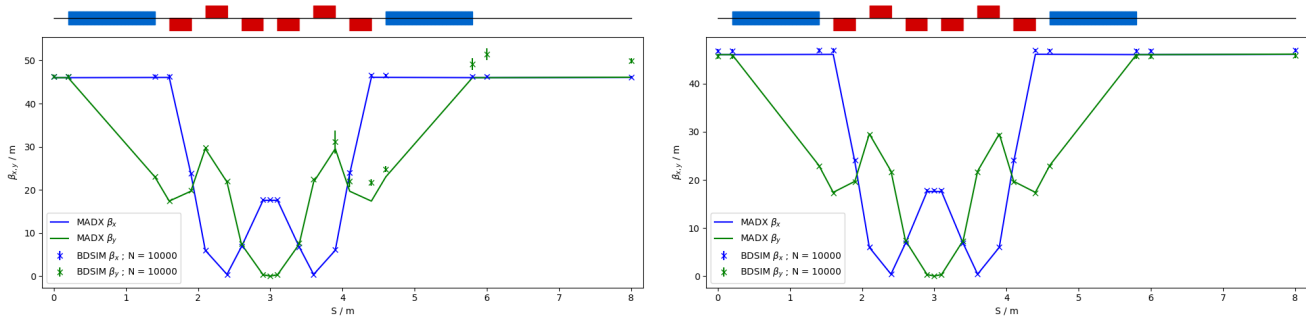636 in-vivo beam line is 15.6 m in length.

Figure 9. Comparison of MAD-X and BDSIM simulation of 40 MeV (left) and nominal 127 MeV (right) proton beam passing through the high energy in-vitro arc simulated with 10^4 particles (in BDSIM).
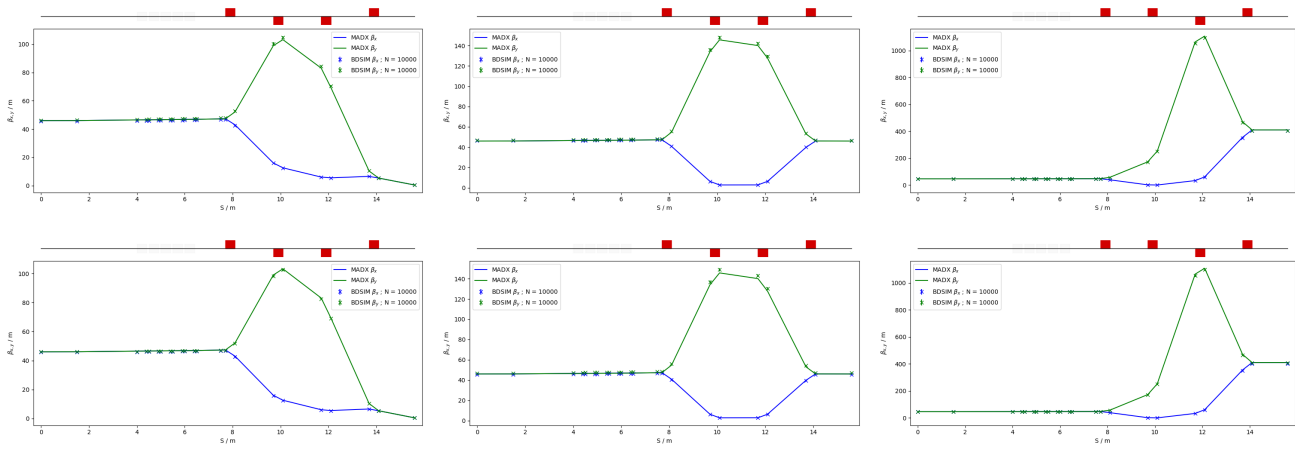

Figure 10. MAD-X and BDSIM simulations of the in-vivo beam line for a 40 MeV proton beam (top row) and a nominal 127 MeV proton beam (bottom row) with quadrupoles matched to $\beta_{x,y} = 0.46$ m (left), $\beta_{x,y} = 46$ m (middle) and $\beta_{x,y} = 410$ m (right) for 10^4 particles.

The design is flexible in matching the various $\beta_{x,y}$ values given in table 4, but is not able to match the smallest target value of $\beta_{x,y} = 0.039$ m for the pessimistic scenario, which is very challenging. To verify that the optics design could provide the required beam sizes, simulations were performed with BDSIM using an input Gaussian beam generated with the Twiss β values given in tables 4. Figure 10 shows the results of simulations for a 40 MeV proton beam and a nominal emittance 127 MeV proton beam matched in order to obtain beam sizes of 1 mm, 10 mm and 30 mm. GPT was used to investigate the effects of space-charge. These simulations show discrepancies compared to the BDSIM simulations. These discrepancies can be compensated for by adjusting the strengths of the quadrupoles in the matching section in the extraction line.

3.5 Instrumentation

Commercial off-the-shelf (COTS) instrumentation will be used for Stages 1 and 2 of LhARA wherever possible. However, the characteristics of the beam (e.g. very high charge per bunch, low to moderate energy) will require some custom solutions to be developed. The authors are developing two concepts, termed SciWire and SmartPhantom, for the low- and high-energy in-vitro end stations respectively. These detectors can also be used for beam diagnostics. This new instrumentation may find application at other facilities. Instrumentation for the detection of secondary particles due to the interaction of the beam with

654 tissue is not discussed here but is an important area that will be studied in the future.
655

3.5.1 SciWire

657 For the Stage 1 beam, the maximum proton energy is 15 MeV. Shot-to-shot characterisation of the beam is
658 essential and requires the use of a very thin detector with a fast response. The SciWire is being developed to
659 address this [Kurup (2019)]. A SciWire plane consists of two layers of 250 μm square-section scintillating
660 fibres, with the fibre directions in the two layers orthogonal to each other. This gives a 2D beam-profile
661 measurement. Using multiple planes might also give energy loss information. Detection of the light from
662 SciWire fibres may be by CMOS camera, or using photodiodes. If the instrumentation is sufficiently fast, it
663 could be used to derive feedback signals for beam tuning.
664

3.5.2 SmartPhantom

666 To study in real time the dose profile of Stage 2 beams, the SmartPhantom [Barber (2018)] is being
667 developed. This is a water-filled phantom, which is instrumented with planes of scintillating fibres, by
668 which to infer the dose distribution with distance. The detection elements of the SmartPhantom are 250 μm
669 diameter, round scintillating fibres. Each fibre station consist of two planes of fibres, in which the fibre
670 directions are orthogonal. Five fibre stations are arranged in the phantom in front of the cell-culture flask.
671 The fibres may be coupled to photodiodes, or a CMOS camera. Simulations in GEANT4 are being used to
672 develop analysis techniques by which to predict the position of the Bragg peak shot-by-shot. The beam
673 profile and dose delivered can then be calculated in real time. The key emphasis is to be able to derive these
674 parameters from shot- by- shot data, and not purely from simulations.
675

3.5.3 Beam line Instrumentation

677 The instrumentation requirement begins with the Ti:Sapphire laser. The laser focal spot will be
678 characterised using a camera-based system and high-speed wavefront measurements [Wang (2014)]
679 from COTS vendors.

680 For the Stage 1 beam line, beam position monitors (BPMs) will be needed for beam steering. Because
681 of the low beam energy, non-intercepting BPMs using capacitive pickup buttons will be used. Custom
682 pickups will be needed to match the beam pipe geometry but COTS electronics are available. The beam
683 current will be monitored near the end of each beam line, using integrating current toroids (ICT), backed
684 up with the option of insertable multi-layer Faraday cups (MLFC) to give absolute beam current and energy
685 measurements. Beam profiles could be measured by SEM grids on both Stage 1 and Stage 2 beam lines.
686 For Stage 1, these monitors will be mounted on pneumatic actuators to avoid scattering. Each end station
687 could be equipped with insertable "pepper-pot" emittance monitors and a transverse deflection cavity with
688 fluorescent screen could be provided for bunch shape measurements.

689 The BPMs on the FFA will require pickup designs suitable for the unusual, wide and shallow, vacuum
690 vessel. The FFA at the KURNS facility in Kyoto is of a similar layout [Uesugi (2018)] and uses a kicker
691 and capacitive pickup for to perform tune measurements in each transverse direction. A minimum of one
692 BPM every second cell will be used in the FFA so that the tune can be matched. BPMs will also be required
693 close to the injection and extraction septa. The BPM system may be able to use COTS electronics, but the
694 pickups will be based on the KURNS design of multiple electrodes arranged across the vacuum vessel
695 width.

696 The DAQ needs to be able to store calibration data and apply corrections in real time. It is necessary to
697 be able to find the beam centre from a profile, even when the profile may be non-Gaussian and possibly

698 asymmetric. FPGAs can be used to perform fast fitting and pattern recognition of beam profiles. The
699 instrumentation will be integrated with the accelerator control system to be able to provide fast feedback
700 and adjustment of the beam parameters in real time.

701

3.6 Biological end stations

703 In order to deliver a successful radiobiological research programme, high-end and fully equipped in-vitro
704 and in-vivo end-stations will be housed within the LhARA facility. The two in-vitro end-stations (high
705 and low energy) will contain vertically delivered beam lines which will be used for the irradiation of 2D
706 monolayer and 3D cells systems (spheroids and patient-derived organoids) in culture. The beam line within
707 the end-stations will be housed in sealed units that will be directly sourced with appropriate gases (carbon
708 dioxide and nitrogen), allowing for the cells within culture plates to be incubated for a short time in stable
709 conditions prior to and during irradiation. This will also enable the chamber to act, where necessary, as
710 a hypoxia unit (0.1–5% oxygen concentration). Furthermore, these sealed units will contain robotics to
711 enable simple movement of the numerous cell culture plates housed within to be placed into and taken
712 away from the beam.

713 The in-vitro end-stations will be located within a research laboratory equipped with up-to-date and
714 state-of-the-art facilities. This, coupled with two separate end-stations and multiple workspaces, will enable
715 multiple groups of researchers to perform productive and high-quality biological research. The laboratory
716 will include all the vital equipment for bench-top science, sample processing and analysis (e.g. refrigerated
717 centrifuges and light/fluorescent microscopes), along with the equipment required for contaminant-free cell
718 culture (e.g. humidified CO_2 cell culture incubators, Class II biological safety cabinets), and for the storage
719 of biological samples and specimens (e.g. -20 °C / -80 °C freezers and fridges). The laboratory will also
720 house an X-ray irradiator (allowing direct RBE comparisons between conventional photon irradiation, and
721 the proton and carbon ions delivered by the accelerator), hypoxia chamber (for long-term hypoxia studies),
722 a robotic workstation (handling and processing of large sample numbers, assisting in high-throughput
723 screening experiments), and an ultra-pure water system. These facilities will enable a myriad of biological
724 end-points to be investigated in both normal- and tumour-cell models not only from routine clonogenic
725 survival and growth assays, but will expand significantly on more complex end-points (e.g. inflammation,
726 angiogenesis, senescence and autophagy) as these experiments are difficult to perform at current clinical
727 research beams due to limited time and facilities.

728 The in-vivo end-station, housed on the basement floor, will be served with high-energy proton and carbon
729 ions capable of penetrating deeper into tissues allowing the irradiation of whole animals. The ability to
730 perform in-vivo preclinical studies is vital for the future effective translation of the research into human
731 cancer patients where optimum treatment strategies and reduction of side-effects can be defined. The
732 in-vivo end-station will allow the irradiation of a number of small-animal models (e.g. xenograft mouse
733 and rat models) which can further promote an examination of particular ions on the appropriate biological
734 end-points (e.g. tumour growth and normal tissue responses). The end-station will contain a small-animal
735 handling area which will allow for the anaesthetisation of animals prior to irradiation. To enable the
736 irradiation of small target volumes with a high level of precision and accuracy, an image guidance system
737 (e.g. computed tomography) will be available. The animals will subsequently be placed in temperature-
738 controlled holder tubes enabling the correct positioning of the relevant irradiation area in front of the
739 beam line. The beam size is sufficient to give flexibility in the different irradiation conditions, in particular
740 through passive scattering, pencil-beam scanning, and micro-beam illumination, to be investigated at both
741 conventional and FLASH dose rates. It is envisaged that the animals will be taken off-site post-irradiation

742   to a nearby animal-holding facility for a follow-up period where biological measurements will be conducted.

743

3.7   Infrastructure and integration

745   The LhARA facility will encompass two floors of roughly 42 m in length and 18 m wide. The ground
746   floor will contain the laser, accelerator, and in-vivo end station while the first floor will house the laboratory
747   area and the two in-vitro end stations. The entire facility will require radiation protection in the form of
748   concrete shielding, which will delineate the facility into three principal areas: a radiation-controlled access
749   area, a laser controlled access area and a laboratory limited-access area.

750   It is assumed that LhARA will be built at an STFC National Laboratory or equivalent research institute
751   which has an established safety-management system and culture in place. At STFC, a comprehensive set of
752   Safety Codes has been developed to cover the hazards associated with working in such an environment.
753   STFC Safety Codes applicable to LhARA include: risk management, construction, biological safety,
754   working with lasers, working with time-varying electro-magnetic fields, management of ionising radiation
755   at work and electrical safety. In practice at STFC, these codes are backed-up by the knowledge, skills and
756   experience of staff and by appointed responsible persons such as Radiation Protection Advisors, Laser
757   Responsible Officers and Authorising Engineers. In addition, STFC operates many facilities that encompass
758   the same hazards as LhARA, which for lasers include the Gemini Target Areas 2 and 3 [STFC (2019a)]
759   as well as the new EPAC (Extreme Photonics Application Centre) [STFC (2019b)] and for accelerators
760   include FETS (Front End Test Stand) [Letchford et al. (2015)] and the ISIS Neutron and Muon Source
761   [STFC (2019c)]. Safety systems will be required for LhARA, which will include Class II biological safety
762   cabinets and sealed plates prior to experiments.

763   For a facility such as LhARA, radiation safety is a primary concern and all work will be completed
764   under Regulation 8 of the Ionising Radiations Regulations 2017 (IRR17) [HSE (2018)], which requires a
765   radiation risk assessment before commencing a new work activity involving ionising radiation.

766   The infrastructure and integration of the LhARA facility will require R&D in four key areas: risk analysis
767   (project risks), risk assessments (safety risks), radiation simulations, and controls development. The risk
768   analysis will cover all aspects of the facility, such as funding and resource availability, not just technical
769   risks. A safety-risk assessment will be performed to describe and control all potential safety risks in the
770   facility. The safety-risk assessment will, to a reasonable degree, identify all pieces of equipment that
771   require safety mitigations and identify control measures that must be put in place. Coupled closely with the
772   safety-risk assessment, radiation simulations will be developed to characterise the radiation hazards in and
773   around the LhARA facility. The last area to require R&D will be the control systems. It is expected that the
774   facility will use the Experimental Physics and Industrial Control System (EPICS), which can be further
775   developed at this stage.

776

4   PERFORMANCE

777   The dose distributions delivered to the end stations was evaluated using BDSIM. Figure 11 shows the
778   energy lost by the beam as it enters the low-energy, in-vitro end station. The beam passes through the
779   vacuum window, a layer of scintillating fibre and then traverses a 5 mm air gap. The beam then enters
780   the cell-sample container, assumed to be polystyrene on which a layer of cells, which supports $30\,\mu$m
781   thick layer of cells, modelled using the Geant4 material "G4_SKIN_ICRP" [NIST (2017)]. The transverse
782   momentum of protons in the beam was assumed to be Gaussian distributed, with a lateral spread small
783   enough for the beam to be fully contained within the required spot size of 3 cm. Figure 11 shows a proton
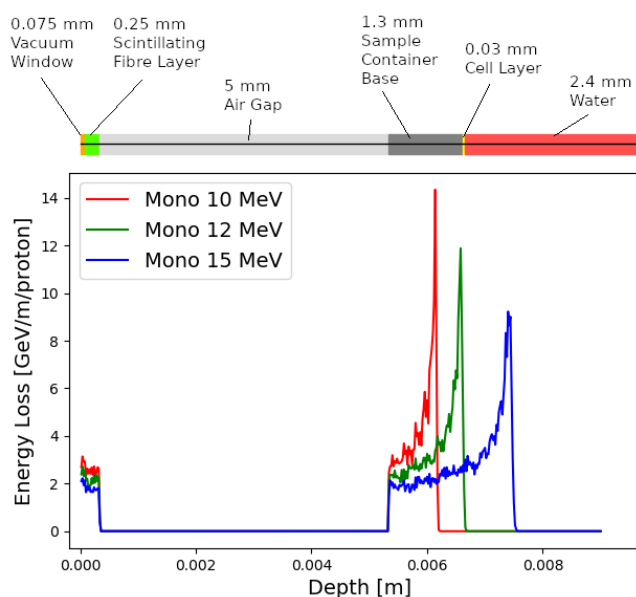
Figure 11. Energy loss as a function of depth in the low-energy in-vitro end station for three mono-energetic proton energies: 10 MeV; 12 MeV; and 15 MeV. Each beam was simulated using 10^4 particles at the start of the beam line.

784   beam with 10 MeV kinetic energy does not reach the cell. The Bragg peak of a 12 MeV proton beam
785   is located close to the cell layer, while a 15 MeV beam, maximum energy specified for delivery to the
786   low-energy in-vitro end station, has a Bragg peak located beyond the cell layer. LhARA's ability to deliver
787   various energies will allow the investigation of radiobiological effects for irradiations using different parts
788   of the Bragg peak, effectively varying the LET across the sample.

789   The maximum dose that can be delivered was evaluated for a variety of beam energies. The dose was
790   estimated by calculating the energy deposited in a volume the size of the sensitive volume of a PTW 23343
791   Markus ion chamber placed at the position of the Bragg peak. The volume of the cylindrical chamber
792   has a radius of 2.65 mm and a depth of 2 mm, giving a volume of about 4.4×10^{-8} m^3. The total energy
793   deposited into the volume was recorded and converted into dose in units of Gray.

794   For the low-energy in-vitro end station the minimum spot size is specified to have a diameter of 10 mm,
795   which is larger than the area of the chamber. A single shot of 10^9 protons at 12 MeV with the minimum
796   design spot size deposits 2.98×10^{-4} J in the chamber volume, corresponding to a dose of 6.75 Gy. For this
797   simulation, the thickness of the sample container was reduced so that the Bragg peak was positioned within
798   the chamber volume. For a bunch width of 2 ns the maximum instantaneous dose rate is 3.37×10^9 Gy/s
799   and the average dose rate is 67.5 Gy/s assuming a repetition rate of 10 Hz. A single shot of 10^9 protons at
800   15 MeV deposits 5.40×10^{-4} J in the chamber volume corresponding to a dose of 12.23 Gy. This gives an
801   instantaneous dose rate of 6.12×10^9 Gy/s and an average dose rate of 122 Gy/s.

802   For the high energy in-vitro end station a different setup was used to accommodate the higher energies. A
803   similar design to the low-energy end station was used but with the air gap increased from 5 mm to 5 cm and
804   a water phantom was placed at the end of the air gap instead of a cell culture plate. The water phantom
805   used in the simulation was based upon the PTC T41023 water phantom. In addition, the smaller minimum
806   design beam size of 1 mm was used. A single shot of 10^9 protons at 127 MeV deposits 1.95×10^{-3} J in the
807   chamber at the pristine Bragg peak depth corresponding to a dose of 44.1 Gy, an instantaneous dose rate

Table 5. Summary of expected maximum dose per pulse and dose rates that LhARA can deliver for minimum beam sizes. These estimates are based on Monte Carlo simulations using a bunch width of 2 ns for the instantaneous dose rate and the average dose rate is based on the 10 Hz repetition rate of the laser source.

	12 MeV Protons	15 MeV Protons	127 MeV Protons	33.4 MeV/u Carbon
Dose per pulse	6.75 Gy	12.23 Gy	44.12 Gy	1141.57 Gy
Instantaneous dose rate	3.37×10^9 Gy/s	6.12×10^{10} Gy/s	2.21×10^{10} Gy/s	5.71×10^{11} Gy/s
Average dose rate	67.5 Gy/s	122.3 Gy/s	441.2 Gy/s	11416 Gy/s

808 of 2.21×10^{10} Gy/s and an average dose rate of 441 Gy/s. For a 33.4 MeV/u carbon beam, a single pulse
809 of 10^9 ions deposits a total energy of 5.04×10^{-2} J at the depth of the pristine Bragg peak, leading to an
810 instantaneous dose rate of 5.71×10^{11} Gy/s and a maximum average dose rate of 11.4×10^3 Gy/s.

811 The expected scaled maximum dose rates are summarised in table 5 from the simulations of the dose per
812 pulse, instantaneous dose rate assuming a 2 ns bunch width, and an average dose rate assuming a 10 Hz
813 repetition rate from the laser-driven ion source. The minimum beam size used for the 12 MeV and 15 MeV
814 proton-beam simulations was 1 cm. A 1 mm beam radius was assumed for the 127 MeV proton beam and
815 33.4 MeV/u carbon-ion beam simulations.

816

5 CONCLUSIONS

817 The initial conceptual design of LhARA, the Laser-hybrid Accelerator for Radiobiological Applications,
818 has been described and its performance evaluated in simulations that take into account the key features of
819 the facility. LhARA combines a laser-driven source to create a large flux of protons or light ions which are
820 captured and formed into a beam by strong-focusing plasma lenses thus evading the current space-charge
821 limit on the instantaneous dose rate that can be delivered. Acceleration, performed using a fixed-field
822 alternating-gradient accelerator (FFA), preserves the unique flexibility in the time, spectral and spatial
823 structure of the beam afforded by the laser-driven source. The ability to trigger the laser pulse that initiates
824 the production of protons or ions at LhARA will allow the time structure of the beam to be varied to
825 interrupt the chemical and biological pathways that determine the biological response to ionising radiation.
826 In addition, the almost parallel beam that LhARA will deliver can be varied to illuminate a circular area
827 with a maximum diameter of between 1 cm and 3 cm with an almost uniform dose or focused to a spot with
828 diameter of ~ 1 mm. These features make LhARA the ideally flexible tool for the systematic study of the
829 radiobiology of proton and ion beams.

830 The technologies demonstrated in LhARA have the potential to be developed to make "best in class"
831 treatments available to the many by reducing the footprint of future particle-beam therapy systems. The
832 laser-hybrid approach, therefore, will allow radiobiological studies and eventually radiotherapy to be
833 carried out in completely new regimes, delivering a variety of ion species in a broad range of time structures
834 and spatial configurations at instantaneous dose rates up to and potentially significantly beyond the current
835 ultra-high dose-rate "FLASH" regime.

836 LhARA has the potential to drive a change in clinical practice in the medium term by increasing the
837 wealth of radiobiological knowledge. This enhanced understanding in turn may be used to devise new
838 approaches to decrease radio-toxicity on normal tissue while maintaining, or even enhancing, the tumour-
839 kill probability. This, in combination the demonstration in operation of the laser-hybrid technique, LhARA

840 has the potential to drive a step-change in the clinical practice of proton- and ion-beam therapy.
841

ACKNOWLEDGEMENTS

REFERENCES

850 [Dataset] (2020). Vsim for plasma. `https://www.txcorp.com/vsim`

851 [Dataset] A-SAIL Project (2020). A-sail project. `https://www.qub.ac.uk/`
852 `research-centres/A-SAILProject/`

853 Amin, T., Barlow, R., Ghithan, S., Royb, G., and Schuhb, S. (2018). Formation of a uniform ion beam
854 using octupole magnets for bioleir facility at cern. *JINST* 13, P04016

855 Atun, R., Jaffray, D. A., Barton, M. B., Bray, F., Baumann, M., Vikram, B., et al. (2015). Expanding
856 global access to radiotherapy. *The Lancet Oncology* 16, 1153 – 1186. doi:https://doi.org/10.1016/
857 S1470-2045(15)00222-3

858 Aurand, B., Grieser, S., Toncian, T., Aktan, E., Cerchez, M., Lessmann, L., et al. (2019). A multihertz,
859 kiloelectronvolt pulsed proton source from a laser irradiated continuous hydrogen cluster target. *Physics*
860 *of Plasmas* 26, 073102. doi:10.1063/1.5093287

861 Autin, B., Carli, C., D'Amico, T., Gröbner, O., Martini, M., and Wildner, E. (1998). *BeamOptics:*
862 *A program for analytical beam optics*. Tech. Rep. CERN–98-06, European Organization for
863 Nuclear Research (CERN). `http://inis.iaea.org/search/search.aspx?orig_q=RN:`
864 `30052986`

865 Barber, G. (2018). Outline design and cost estimate for the SmartPhantom. *Unpublished note*

866 Bin, J., Allinger, K., Assmann, W., Dollinger, G., Drexler, G. A., Friedl, A. A., et al. (2012). A laser-
867 driven nanosecond proton source for radiobiological studies. *Applied Physics Letters* 101, 243701.
868 doi:10.1063/1.4769372

869 Bray, F., Ferlay, J., Soerjomataram, I., Siegel, R. L., Torre, L. A., and Jemal, A. (2018). Global cancer
870 statistics 2018: GLOBOCAN estimates of incidence and mortality worldwide for 36 cancers in 185
871 countries. *CA: A Cancer Journal for Clinicians* 68, 394–424. doi:10.3322/caac.21492

872 Bulanov, S., Esirkepov, T., Khoroshkov, V., Kuznetsov, A., and Pegoraro, F. (2002). Oncological
873 hadrontherapy with laser ion accelerators. *Physics Letters A* 299, 240–247. doi:https://doi.org/10.1016/
874 S0375-9601(02)00521-2

875 Carter, R. J., Nickson, C. M., Thompson, J. M., Kacperek, A., Hill, M. A., and Parsons, J. L. (2018).
876 Complex dna damage induced by high linear energy transfer alpha-particles and protons triggers a
877 specific cellular dna damage response. *International Journal of Radiation Oncology*Biology*Physics*
878 100, 776 – 784. doi:https://doi.org/10.1016/j.ijrobp.2017.11.012

879 Chaudhary, P., Gwynne, D., Doria, D., Romagnani, L., Maiorino, C., Padda, H., et al. (2017). Effectiveness
880 of laser accelerated ultra high dose rate protons in DNA DSB damage induction under hypoxic conditions.

In *44th EPS Conference on Plasma Physics, EPS 2017* (European Physical Society (EPS)), vol. 44F. P1.217

Chaudhary, P., Marshall, T. I., Perozziello, F. M., Manti, L., Currell, F. J., Hanton, F., et al. (2014). Relative Biological Effectiveness Variation Along Monoenergetic and Modulated Bragg Peaks of a 62-MeV Therapeutic Proton Beam: A Preclinical Assessment. *International Journal of Radiation Oncology • Biology • Physics* 90, 27–35. doi:10.1016/j.ijrobp.2014.05.010

Cirrone, G. A. P., Margarone, D., Maggiore, M., Anzalone, A., Borghesi, M., Jia, S. B., et al. (2013). ELIMED: a new hadron therapy concept based on laser driven ion beams. In *Laser Acceleration of Electrons, Protons, and Ions II; and Medical Applications of Laser-Generated Beams of Particles II; and Harnessing Relativistic Plasma Waves III*, eds. E. Esarey, C. B. Schroeder, W. P. Leemans, K. W. D. Ledingham, and D. A. Jaroszynski. International Society for Optics and Photonics (SPIE), vol. 8779, 216 – 225. doi:10.1117/12.2026530

Clark, E. L., Krushelnick, K., Davies, J. R., Zepf, M., Tatarakis, M., Beg, F. N., et al. (2000). Measurements of energetic proton transport through magnetized plasma from intense laser interactions with solids. *Phys. Rev. Lett.* 84, 670–673. doi:10.1103/PhysRevLett.84.670

Daido, H., Nishiuchi, M., and Pirozhkov, A. S. (2012). Review of laser-driven ion sources and their applications. *Reports on Progress in Physics* 75, 56401. doi:10.1088/0034-4885/75/5/056401

Dann, S. J. D., Baird, C. D., Bourgeois, N., Chekhlov, O., Eardley, S., Gregory, C. D., et al. (2019). Laser wakefield acceleration with active feedback at 5 hz. *Phys. Rev. Accel. Beams* 22, 041303. doi:10.1103/PhysRevAccelBeams.22.041303

Datta, N. R., Rogers, S., and Bodis, S. (2019). Challenges and Opportunities to Realize "The 2030 Agenda for Sustainable Development" by the United Nations: Implications for Radiation Therapy Infrastructure in Low- and Middle-Income Countries. *International Journal of Radiation Oncology*Biology*Physics* 105, 918–933. doi:https://doi.org/10.1016/j.ijrobp.2019.04.033

De Loos, M. J. and Van der Geer, S. B. (1996). General Particle Tracer: A New 3D Code for Accelerator and Beamline Design

Doria, D., Kakolee, K. F., Kar, S., Litt, S. K., Fiorini, F., Ahmed, H., et al. (2012a). Biological effectiveness on live cells of laser driven protons at dose rates exceeding 10^9 Gy/s. *AIP Advances* 2, 011209. doi:10.1063/1.3699063

Doria, D., Kakolee, K. F., Kar, S., Litt, S. K., Fiorini, F., Ahmed, H., et al. (2012b). Biological effectiveness on live cells of laser driven protons at dose rates exceeding $109 Gy/s$. *AIP Advances* 2, 011209. doi:10.1063/1.3699063

Favaudon, V., Caplier, L., Monceau, V., Pouzoulet, F., Sayarath, M., Fouillade, C., et al. (2014). Ultrahigh dose-rate flash irradiation increases the differential response between normal and tumor tissue in mice. *Science Translational Medicine* 6, 245ra93–245ra93. doi:10.1126/scitranslmed.3008973

Fiorini, F., Kirby, D., Borghesi, M., Doria, D., Jeynes, J. C., Kakolee, K. F., et al. (2011). Dosimetry and spectral analysis of a radiobiological experiment using laser-driven proton beams. *Phys Med Biol* 56, 6969–6982

Fitzmaurice, C., Akinyemiju, T. F., Al Lami, F. H., Alam, T., Alizadeh-Navaei, R., Allen, C., et al. (2018). Global, Regional, and National Cancer Incidence, Mortality, Years of Life Lost, Years Lived With Disability, and Disability-Adjusted Life-Years for 29 Cancer Groups, 1990 to 2016. *JAMA Oncology* 4, 1553. doi:10.1001/jamaoncol.2018.2706

Fourkal, E., Li, J. S., Ding, M., Tajima, T., and Ma, C. M. (2003). Particle selection for laser-accelerated proton therapy feasibility study. *Medical Physics* 30, 1660–1670. doi:10.1118/1.1586268

Fourrier, J., Martinache, F., Meot, F., and Pasternak, J. (2008). Spiral ffag lattice design tools. application to 6-d tracking in a proton-therapy class lattice. *Nucl. Instrum. Meth.* A589, 133–142. doi:10.1016/j.nima.2008.01.082

Gabor, D. (1947). A Space-Charge Lens for the Focusing of Ion Beams. *Nature* 160, 89–90. doi:10.1038/160089b0

Gauthier, M., Curry, C. B., Göde, S., Brack, F.-E., Kim, J. B., MacDonald, M. J., et al. (2017). High repetition rate, multi-mev proton source from cryogenic hydrogen jets. *Applied Physics Letters* 111, 114102. doi:10.1063/1.4990487

Giovannini, G., Böhlen, T., Cabal, G., Bauer, J., Tessonnier, T., Frey, K., et al. (2016). Variable RBE in proton therapy: comparison of different model predictions and their influence on clinical-like scenarios. *Radiation Oncology* 11, 68. doi:10.1186/s13014-016-0642-6

Grote, H. and Schmidt, F. (2003). MAD-X: An upgrade from MAD8. *Conf. Proc. C* 030512, 3497

HSE (2018). *Work with ionising radiation - Ionising Radiations Regulations 2017* (Crown)

IBA (2019). Flash irradiation delivered in a clinical treatment room `https://iba-worldwide.com/content/pt/proton-flash-irradiation-delivered-clinical-treatment-room`

Jones, B., McMahon, S. J., and Prise, K. M. (2018). The Radiobiology of Proton Therapy: Challenges and Opportunities Around Relative Biological Effectiveness. *Clinical Oncology* 30, 285–292. doi:10.1016/j.clon.2018.01.010.

Karger, C. P. and Peschke, P. (2017). RBE and related modeling in carbon-ion therapy. *Physics in Medicine & Biology* 63, 01TR02. doi:10.1088/1361-6560/aa9102

[Dataset] Kirschner, J., Mutný, M., Hiller, N., Ischebeck, R., and Krause, A. (2019). Adaptive and safe bayesian optimization in high dimensions via one-dimensional subspaces

Kraft, S. D., Richter, C., Zeil, K., Baumann, M., Beyreuther, E., Bock, S., et al. (2010a). Dose–dependent biological damage of tumour cells by laser–accelerated proton beams. *New Journal of Physics* 12, 085003. doi:10.1088/1367-2630/12/8/085003

Kraft, S. D., Richter, C., Zeil, K., Baumann, M., Beyreuther, E., Bock, S., et al. (2010b). Dose-dependent biological damage of tumour cells by laser-accelerated proton beams. *New Journal of Physics* 12, 85003. doi:10.1088/1367-2630/12/8/085003

Krest, D., Laslett, L., Jones, L. W., Symon, K., and Terwilliger, K. (1956). *Fixed field alternating gradient particle accelerators*. Tech. Rep. MURA-109, MURA-DWK-KRS-LJL-LWJ-KMT-3, Midwestern Universities Research Association (MURA)

Kurup, A. (2019). Diagnostics for LhARA. *Low energy ion beam diagnostics workshop, Imperial College*

Lagrange, J. B., Appleby, R. B., Garland, J. M., Pasternak, J., and Tygier, S. (2018). Racetrack FFAG muon decay ring for nuSTORM with triplet focusing. *JINST* 13, P09013. doi:10.1088/1748-0221/13/09/P09013

Letchford, A. et al. (2015). Status of the ral front end test stand. In *IPAC*

Loeffler, J. S. and Durante, M. (2013). Charged particle therapy—optimization, challenges and future directions. *Nature Reviews Clinical Oncology* 10, 411–424. doi:10.1038/nrclinonc.2013.79

Lühr, A., von Neubeck, C., Krause, M., and Troost, E. G. C. (2018). Relative biological effectiveness in proton beam therapy – Current knowledge and future challenges. *Clinical and Translational Radiation Oncology* 9, 35–41. doi:10.1016/j.ctro.2018.01.006

Malka, V., Fritzler, S., Lefebvre, E., d'Humières, E., Ferrand, R., Grillon, G., et al. (2004). Practicability of proton therapy using compact laser systems. *Medical Physics* 31, 1587–1592. doi:10.1118/1.1747751

969   Manti, L., Perozziello, F., Borghesi, M., Candiano, G., Chaudhary, P., Cirrone, G., et al. (2017a). The
970   radiobiology of laser-driven particle beams: focus on sub-lethal responses of normal human cells. *Journal*
971   *of Instrumentation* 12, C03084–C03084. doi:10.1088/1748-0221/12/03/c03084

972   Manti, L., Perozziello, F. M., Borghesi, M., Candiano, G., Chaudhary, P., Cirrone, G. A., et al. (2017b).
973   The radiobiology of laser-driven particle beams: Focus on sub-lethal responses of normal human cells.
974   *Journal of Instrumentation* 12. doi:10.1088/1748-0221/12/03/C03084

975   Margarone, D., Cirrone, G. A. P., Cuttone, G., Amico, A., Andò, L., Borghesi, M., et al. (2018).
976   Elimaia: A laser–driven ion accelerator for multidisciplinary applications. *Quantum Beam Science* 2.
977   doi:10.3390/qubs2020008

978   Margarone, D., Velyhan, A., Dostal, J., Ullschmied, J., Perin, J. P., Chatain, D., et al. (2016). Proton
979   acceleration driven by a nanosecond laser from a cryogenic thin solid-hydrogen ribbon. *Phys. Rev. X* 6,
980   041030. doi:10.1103/PhysRevX.6.041030

981   Masood, U., Bussmann, M., Cowan, T. E., Enghardt, W., Karsch, L., Kroll, F., et al. (2014). A
982   compact solution for ion beam therapy with laser accelerated protons. *Applied Physics B* 117, 41–52.
983   doi:https://doi.org/10.1007/s00340-014-5796-z

984   Masood, U., Cowan, T. E., Enghardt, W., Hofmann, K. M., Karsch, L., Kroll, F., et al. (2017). A
985   light-weight compact proton gantry design with a novel dose delivery system for broad-energetic
986   laser-accelerated beams. *Physics in Medicine & Biology* 62, 5531–5555. doi:10.1088/1361-6560/aa7124

987   Meusel, O., Droba, M., Glaeser, B., and Schulte, K. (2013). Experimental studies of stable confined electron
988   clouds using Gabor lenses. *Conf. Proc. C* 1206051, 157–160. doi:10.5170/CERN-2013-002.157

989   Morrison, J. T., Feister, S., Frische, K. D., Austin, D. R., Ngirmang, G. K., Murphy, N. R., et al. (2018).
990   MeV proton acceleration at kHz repetition rate from ultra-intense laser liquid interaction. *New Journal*
991   *of Physics* 20, 22001. doi:10.1088/1367-2630/aaa8d1

992   Nevay, L. J. et al. (2020). Bdsim: An accelerator tracking code with particle-matter interactions. *Computer*
993   *Physics Communications* , 107200

994   NIST (2017). *NIST Standard Reference Database 124* (National Institute of Standards and Technology).
995   doi:https://dx.doi.org/10.18434/T4NC7P

996   Noaman-ul Haq, M., Ahmed, H., Sokollik, T., Yu, L., Liu, Z., Yuan, X., et al. (2017). Statistical analysis of
997   laser driven protons using a high-repetition-rate tape drive target system. *Phys. Rev. Accel. Beams* 20,
998   041301. doi:10.1103/PhysRevAccelBeams.20.041301

999   Obst, L., Göde, S., Rehwald, M., Brack, F.-E., Branco, J., Bock, S., et al. (2017). Efficient laser-driven
1000   proton acceleration from cylindrical and planar cryogenic hydrogen jets. *Scientific Reports* 7, 10248.
1001   doi:10.1038/s41598-017-10589-3

1002   Osmic, F., Feurstein, M., Gyorgy, A., Kerschbaum, A., Repovz, M., Schwarz, S., et al. (2012). Overview
1003   of the Beam diagnostics in the Medaustron Accelerator:Design choices and test Beam commissioning.
1004   *Conf. Proc.* C1205201, MOPPR002. 3 p

1005   Paganetti, H. (2014). Relative biological effectiveness (RBE) values for proton beam therapy. Variations as
1006   a function of biological endpoint, dose, and linear energy transfer. *Phys. Med. Biol.* 59, R419

1007   Paganetti, H. and van Luijk, P. (2013). Biological considerations when comparing proton therapy with
1008   photon therapy. *Seminars in Radiation Oncology* 23, 77 – 87. doi:https://doi.org/10.1016/j.semradonc.
1009   2012.11.002. Controversies in Proton Therapy

1010   Planche, T., Fourrier, J., Lancelot, J. L., Meot, F., Neuveglise, D., and Pasternak, J. (2009). Design of a
1011   prototype gap shaping spiral dipole for a variable energy protontherapy FFAG. *Nucl. Instrum. Meth.*
1012   A604, 435–442. doi:10.1016/j.nima.2009.02.026

Pommarel, L., Vauzour, B., Mégnin-Chanet, F., Bayart, E., Delmas, O., Goudjil, F., et al. (2017). Spectral and spatial shaping of a laser-produced ion beam for radiation-biology experiments. *Physical Review Accelerators and Beams* 20, 1–10. doi:10.1103/PhysRevAccelBeams.20.032801

Pozimski, J. and Aslaninejad, M. (2013). Gabor lenses for capture and energy selection of laser driven ion beams in cancer treatment. *Laser and Particle Beams* 31, 723—-733. doi:10.1017/S0263034613000761

Prezado, Y., Jouvion, G., Hardy, D., Patriarca, A., Nauraye, C., Bergs, J., et al. (2017). Proton minibeam radiation therapy spares normal rat brain: Long-Term Clinical, Radiological and Histopathological Analysis. *Scientific Reports* 7, 14403. doi:10.1038/s41598-017-14786-y

[Dataset] PTCOG (2020). Particle Therapy Co-Operative Group. `https://www.ptcog.ch/index.php/patient-statistics`

Reiser, M. (1989). Comparison of gabor lens, gas focusing, and electrostatic quadrupole focusing for low-energy ion beams. In *Proceedings of the 1989 IEEE Particle Accelerator Conference, . 'Accelerator Science and Technology*. 1744–1747 vol.3

Romano, F., Schillaci, F., Cirrone, G., Cuttone, G., Scuderi, V., Allegra, L., et al. (2016). The elimed transport and dosimetry beamline for laser-driven ion beams. *Nuclear Instruments and Methods in Physics Research Section A: Accelerators, Spectrometers, Detectors and Associated Equipment* 829, 153–158. doi:https://doi.org/10.1016/j.nima.2016.01.064. 2nd European Advanced Accelerator Concepts Workshop – EAAC 2015

Snavely, R. A., Key, M. H., Hatchett, S. P., Cowan, T. E., Roth, M., Phillips, T. W., et al. (2000). Intense high-energy proton beams from petawatt-laser irradiation of solids. *Phys. Rev. Lett.* 85, 2945–2948. doi:10.1103/PhysRevLett.85.2945

[Dataset] STFC (2019a). The astra gemini facility. `https://www.clf.stfc.ac.uk/Pages/The-Astra-Gemini-Facility.aspx`

[Dataset] STFC (2019b). Introducing the extreme photonics applications centre. `https://www.clf.stfc.ac.uk/Pages/EPAC-introduction-page.aspx`

[Dataset] STFC (2019c). Isis neutron and muon source. `https://stfc.ukri.org/research/our-science-facilities/isis-neutron-and-muon-source/`

Streeter, M. J. V., Dann, S. J. D., Scott, J. D. E., Baird, C. D., Murphy, C. D., Eardley, S., et al. (2018). Temporal feedback control of high-intensity laser pulses to optimize ultrafast heating of atomic clusters. *Applied Physics Letters* 112, 244101. doi:10.1063/1.5027297

Symon, K. R., Kerst, D. W., Jones, L. W., Laslett, L. J., and Terwilliger, K. M. (1956). Fixed-field alternating-gradient particle accelerators. *Phys. Rev.* 103, 1837–1859. doi:10.1103/PhysRev.103.1837

Systems, V. M. (2020). Flashforward consortium `https://www.varian.com/about-varian/research/flashforward-consortium`

Tanigaki, M., Mori, Y., Inoue, M., Mishima, K., Shiroya, S., Ishi, Y., et al. (2006). Present status of the ffag accelerators in kurri for ads study. In *EPAC 2006 - Contributions to the Proceedings*

The LhARA consortium (2020). *The Laser-hybrid Accelerator for Radiobiological Applications*. Tech. Rep. CCAP-TN-01. `https://ccap.hep.ph.ic.ac.uk/trac/raw-attachment/wiki/Research/DesignStudy/PreCDR/Review/2020-03-31-LhARA_pre_CDR-d2.0.pdf`

[Dataset] The World Health Organisation (2020). Cancer. `https://www.who.int/news-room/fact-sheets/detail/cancer`

Tsoupas, N. et al. (1991). Uniform beam distributions using octupoles. *Proceedings of PAC 1991* , 1695–1697

Uesugi, T. (2018). Betatron Tune Measurement . *FFA School, Osaka*

Urakabe, E. et al. (1999). Beam-profile control using an octupole magnet. *Jpn. J. Appl. Phys.* 38, 6145–6149

Vitti, E. T. and Parsons, J. L. (2019a). The radiobiological effects of proton beam therapy: Impact on dna damage and repair. *Cancers* 11. doi:10.3390/cancers11070946

Vitti, E. T. and Parsons, J. L. (2019b). The radiobiological effects of proton beam therapy: Impact on dna damage and repair. *Cancers* 11, 946. doi:10.3390/cancers11070946

Vozenin, M. C., De Fornel, P., Petersson, K., Favaudon, V., Jaccard, M., Germond, J. F., et al. (2019). The Advantage of FLASH Radiotherapy Confirmed in Mini–pig and Cat–cancer Patients. *Clin. Cancer Res.* 25, 35–42. doi:10.1158/1078-0432

Wang, H. (2014). Wavefront measurement techniques used in high power lasers. *High Power Laser Science and Engineering* 2

Wiggins, S. M., Boyd, M., Brunetti, E., Butler, N. M. H., Feehan, J. S., Gray, R. J., et al. (2019). Application programmes at the Scottish Centre for the Application of Plasma-based Accelerators (SCAPA). In *Relativistic Plasma Waves and Particle Beams as Coherent and Incoherent Radiation Sources III*, eds. D. A. Jaroszynski and M. Hur. International Society for Optics and Photonics (SPIE), vol. 11036, 93 – 103. doi:10.1117/12.2520717

Wilkens, J. J. and Oelfke, U. (2004). A phenomenological model for the relative biological effectiveness in therapeutic proton beams. *Physics in Medicine and Biology* 49, 2811–2825. doi:10.1088/0031-9155/49/13/004

Yogo, A., Maeda, T., Hori, T., Sakaki, H., Ogura, K., Nishiuchi, M., et al. (2011). Measurement of relative biological effectiveness of protons in human cancer cells using a laser-driven quasimonoenergetic proton beamline. *Applied Physics Letters* 98, 053701. doi:10.1063/1.3551623

Yonemura, Y., Arima, H., Ikeda, N., Ishibashi, K., Maehata, K., Noro, T., et al. (2008). Status of center for accelerator and beam applied science of kyushu university. *EPAC 2008 - Contributions to the Proceedings*

Zeil, K., Baumann, M., Beyreuther, E., Burris-Mog, T., Cowan, T. E., Enghardt, W., et al. (2013a). Dose–controlled irradiation of cancer cells with laser-accelerated proton pulses. *Applied Physics B* 110, 437–444. doi:https://doi.org/10.1007/s00340-012-5275-3

Zeil, K., Baumann, M., Beyreuther, E., Burris-Mog, T., Cowan, T. E., Enghardt, W., et al. (2013b). Dose-controlled irradiation of cancer cells with laser-accelerated proton pulses. *Applied Physics B* 110, 437–444. doi:10.1007/s00340-012-5275-3

Zlobinskaya, O., Siebenwirth, C., Greubel, C., Hable, V., Hertenberger, R., Humble, N., et al. (2014). The effects of ultra–high dose rate proton irradiation on growth delay in the treatment of human tumor xenografts in nude mice. *Radiation Research* 181, 177–183. doi:10.1667/RR13464.1